

# The SRG/eROSITA All-Sky Survey

## SRG/eROSITA cross-calibration with Chandra and XMM-Newton using galaxy cluster gas temperatures

K. Migkas<sup>1,2,3</sup>, D. Kox<sup>2</sup>, G. Schellenberger<sup>4</sup>, A. Veronica<sup>2</sup>, F. Pacaud<sup>2</sup>, T. H. Reiprich<sup>2</sup>, Y. E. Bahar<sup>5</sup>, F. Balzer<sup>5</sup>, E. Bulbul<sup>5</sup>, J. Comparat<sup>5</sup>, K. Dennerl<sup>5</sup>, M. Freyberg<sup>5</sup>, C. Garrel<sup>5</sup>, V. Ghirardini<sup>5</sup>, S. Grandis<sup>6</sup>, M. Kluge<sup>5</sup>, A. Liu<sup>5</sup>, M. E. Ramos-Ceja<sup>5</sup>, J. Sanders<sup>5</sup>, X. Zhang<sup>5</sup>

<sup>1</sup> Leiden Observatory, Leiden University, PO Box 9513, 2300 RA Leiden, the Netherlands

<sup>2</sup> Argelander-Institut für Astronomie, Universität Bonn, Auf dem Hügel 71, 53121 Bonn, Germany

<sup>3</sup> SRON Netherlands Institute for Space Research, Niels Bohrweg 4, NL-2333 CA Leiden, the Netherlands

<sup>4</sup> Center for Astrophysics | Harvard & Smithsonian, 60 Garden Street, Cambridge, MA 02138, USA

<sup>5</sup> Max Planck Institute for Extraterrestrial Physics, Gießenbachstraße 1, 85748 Garching bei München, Germany

<sup>6</sup> Universität Innsbruck, Institut für Astro- und Teilchenphysik, Technikerstr. 25/8, 6020 Innsbruck, Austria  
e-mail: kmigkas@strw.leidenuniv.nl

Received date

### ABSTRACT

Galaxy cluster gas temperatures ( $T$ ) play a crucial role in many cosmological and astrophysical studies. However, it has been shown that  $T$  measurements can significantly vary between different X-ray telescopes. These  $T$  biases can propagate to several cluster applications for which  $T$  can be used, such as measuring hydrostatic cluster masses and constraining the angular variation of cosmological parameters. Thus, it is important to accurately cross-calibrate X-ray instruments to account for systematic biases. In this work, we present the cross-calibration between Spectrum Roentgen Gamma/eROSITA (SRG/eROSITA) and Chandra/ACIS, and between SRG/eROSITA and XMM-Newton/EPIC, using for the first time a large sample of galaxy cluster  $T$ . To do so, we use the first eROSITA All-Sky Survey data and the preliminary extremely expanded High FLUX Galaxy Cluster Sample, a large X-ray flux-limited cluster catalog. We spectroscopically measure X-ray  $T$  for 186 independent cluster regions with both SRG/eROSITA and Chandra/ACIS in a self-consistent way, for three energy bands; 0.7-7 keV (full), 0.5-4 keV (soft), and 1.5-7 keV (hard). We do the same with SRG/eROSITA and XMM-Newton/EPIC for 71 different cluster regions and all three bands. We find that SRG/eROSITA measures systematically lower  $T$  than the other two instruments, with hotter clusters deviating more than cooler ones. For the full band, SRG/eROSITA returns 20% and 14% lower  $T$  than Chandra/ACIS and XMM-Newton/EPIC respectively, when the two latter instruments measure  $k_B T \approx 3$  keV each. The discrepancy increases to 38% and 32% when Chandra/ACIS and XMM-Newton/EPIC measure  $k_B T \approx 10$  keV respectively. On the other hand, the discrepancy becomes milder for low- $T$  galaxy groups. Moreover, a broken power law fit demonstrates that there is a break at the SRG/eROSITA-Chandra/ACIS scaling relation at  $k_B T \approx 1.7 - 2.7$  keV, depending on the energy band. The soft band shows a marginally lower discrepancy than the full band. In the hard band, the cross-calibration of SRG/eROSITA and the instruments show very strong differences. We tested several possible systematic biases (such as multiphase cluster gas, Galactic absorption, non-Gaussian scatter, and selection effects) to identify the reason behind the cross-calibration discrepancies but none could significantly alleviate the tension. For now, it is most likely that the systematically lower SRG/eROSITA  $T$  can be attributed to systematic effective area calibration uncertainties; however, the exact role of multiphase cluster gas in the observed  $T$  discrepancies needs to be further investigated. Furthermore, we provide conversion factors between SRG/eROSITA, Chandra/ACIS, and XMM-Newton/EPIC  $T$  which will be beneficial for future cluster studies that combine SRG/eROSITA  $T$  with data from other X-ray instruments. Finally, we also provide conversion functions between the official eRASS1 cluster catalog  $T$  and equivalent core and core-excised Chandra/ACIS and XMM-Newton/EPIC  $T$ .

**Key words.** X-rays: galaxies: clusters – instrumentation: miscellaneous – galaxies: clusters: intracluster medium – techniques: spectroscopic

## 1. Introduction

Galaxy clusters, the largest virialized systems in the Universe, play a critical role in our understanding of various astrophysical and cosmological phenomena. X-ray observations of their most massive baryonic component, the hot intracluster medium (ICM), offer a wealth of information on a wide range of cluster properties. Among these, the ICM temperature ( $T$ ) is particularly valuable, as it is a key factor in many cosmological applications of galaxy clusters.

Widespread cosmological use of galaxy clusters comes through the halo mass function, which puts tight cosmological constraints by modeling the number of cluster haloes per mass and redshift. For such a test, an unbiased modeling of cluster masses is of immense significance. Accurate measurements of  $T$  profiles are used to determine the total hydrostatic mass of clusters, which can be then utilized to constrain cosmology (e.g.,

Schellenberger & Reiprich 2017b)<sup>1</sup>. Moreover, since  $T$  is a low-scattered proxy of the total cluster mass, the latter can also be directly estimated through the mass-temperature scaling relation  $M - T$  (e.g. Lovisari et al. 2015, 2020; Bulbul et al. 2019). Another vital need for high-quality  $T$  measurements arises from the studies of cosmic isotropy with cluster scaling relations (Migkas et al. 2021). Measuring  $T$  does not require any strong cosmological assumptions. As such, the directionality of its correlation with other cosmology-dependent cluster properties constitutes a powerful test of the isotropy of cosmic expansion and the existence of bulk flows in the local Universe. Furthermore, X-ray gas  $T$  measurements are an essential component in a substantial number of astrophysical studies, including assessments of the impact of baryonic feedback on cluster scaling relations (e.g., Mittal et al. 2011), as well as the detection of the Warm Hot Intergalactic Medium (e.g., Werner et al. 2008; Eckert et al. 2015), and many others. It is therefore evident that an unbiased determination of  $T$  is of utter importance for cluster science.

However, it is well established that discrepancies exist between cluster  $T$  measurements obtained by various X-ray telescopes. Schellenberger et al. (2015, S15 hereafter) showed that XMM-Newton/EPIC (hereafter XMM-Newton) returned systematically lower  $T$  values than Chandra/ACIS (hereafter Chandra), using a sample of 64 galaxy clusters observed by both telescopes. This discrepancy was found to increase as a function of  $T$ , from consistency for  $T \approx 1$  keV clusters<sup>2</sup> to a  $\approx 29\%$  higher Chandra  $T$  ( $T_{\text{Chandra}}$  hereafter) for  $T \approx 10$  keV clusters. Furthermore, the temperature difference was stronger in the soft than in the hard X-ray band. Other studies that used only 8-11 clusters found similar, often milder, cluster temperature discrepancies between XMM-Newton, Suzaku, Chandra, and NuSTAR (Nevalainen et al. 2010; Kettula et al. 2013; Wallbank et al. 2022).

If  $T$  disagreements between different X-ray telescopes are not properly taken into account, they can lead to several systematic biases. For instance, S15 showed that using  $T$  values only from XMM-Newton or Chandra without accounting for their cross-calibration issue, results in an 8% difference in the estimated  $\Omega_m$  using hydrostatic masses and the cluster mass function. Moreover, using the Lovisari et al. (2020)  $M - T$  relation, a 10% bias in  $T$  would shift the total cluster masses by 16%. Finally, when testing cosmic isotropy with cluster scaling relations, a 10% systematic difference in  $T$  would cause a 12% shift in  $H_0$ , inducing artificial anisotropies (Migkas et al. 2021).

Cluster science will significantly progress in the following years thanks to the X-ray cluster catalogs provided by the extended ROentgen Survey with an Imaging Telescope Array (eROSITA, Merloni et al. 2012; Predehl et al. 2021). eROSITA was launched on July 2019 on board the Spectrum-Roentgen-Gamma (SRG) space observatory (Sunyaev et al. 2021). It consists of seven telescope modules (TMs), each with 54 nested mirror shells. SRG/eROSITA (hereafter eROSITA) will conduct a 4-year survey, mapping the entire X-ray sky for the first time in the 21st century. Thanks to its large effective area and broad X-ray energy range coverage, eROSITA is expected to detect all massive galaxy clusters ( $M \geq 3 \times 10^{14} M_\odot$ ) in the observable Universe away from the Galactic plane (Merloni et al. 2012; Pillepich et al. 2012). For many thousands of them, precise spectroscopic  $T$  measurements will become possible (Borm et al.

2014), significantly increasing the cluster sample size with available  $T$  values. Thus, a cross-calibration of eROSITA-measured cluster  $T$  with ones from XMM-Newton and Chandra is of utter importance for studies that wish to jointly analyze data coming from these X-ray telescopes.

Recently, Turner et al. (2022) used eight clusters from the eFEDS cluster catalog (Liu et al. 2022) and found that eROSITA returns  $25 \pm 9\%$  lower  $T$  than XMM-Newton in the broad X-ray band, although different energy bands were used for the two instruments. Due to the limited data, the dependence of the discrepancy on cluster temperature could not be constrained. That work provided a first indication of the cross-calibration between these two telescopes but lacked the statistical power for a more precise comparison and a deeper investigation of the discrepancy. Other studies that focused on the eROSITA analysis of single clusters also found temperature discrepancies between eROSITA, XMM-Newton, and Chandra. Sanders et al. (2022) and Whelan et al. (2022) found that eROSITA showed higher  $T$  than XMM-Newton and only slightly lower  $T$  than Chandra for their respective clusters. On the other hand, Veronica et al. (2022) found mildly lower  $T$  with eROSITA than XMM-Newton both in the broad and soft bands for another single cluster. Liu et al. (2023) found that, in the full band, eROSITA measures  $\sim 60\%$  and  $\sim 45\%$  lower  $T$  than Chandra and XMM-Newton respectively. The discrepancy was alleviated when they measured the eROSITA  $T$  ( $T_{\text{eROSITA}}$  hereafter) in the 2-8 keV band, which agreed with the  $T_{\text{Chandra}}$  from the broad X-ray band. These results which are based on single cluster comparisons often contradict each other. This indicates that such individual comparisons are probably not sufficient to characterize the cross-calibration of eROSITA with other X-ray instruments. Due to the non-negligible scatter of these relations, single cluster comparisons are subject to noise fluctuations; thus, one needs large cluster samples to robustly quantify any systematic  $T$  discrepancy. Moreover, most frequently the above studies used different metal abundance and Galactic absorption values for different instruments when comparing their respective  $T$ . To obtain a clearer picture of the eROSITA-Chandra-XMM-Newton cross-calibration, one needs to perform spectral fits with self-consistent "nuisance" parameters across different telescopes so an artificial systematic bias in the  $T$  estimation is avoided.

In this work, we use the data products of the first eROSITA All-Sky survey (eRASS1) to accurately assess the cross-calibration between eROSITA, XMM-Newton, and Chandra. To do so, we measure the cluster gas  $T$  using eRASS1 data for (nearly) all systems included in the preliminary extremely expanded HIGH FLUX Galaxy Cluster Sample (eeHIFLUGCS) catalog, as presented in Migkas et al. (2020, M20 hereafter), and lie in the Western Galactic hemisphere. We measure the core and core-excised  $T$  and metallicity  $Z$  for 120 and 51 clusters with Chandra and XMM-Newton  $T$  measurements respectively, from the same cluster areas and for the 0.7-7 keV energy band. For the majority of these clusters, we also compare the spectral fits for the soft (0.5-4 keV) and hard (1.5-7 keV) X-ray bands. Our results provide clear conversion functions between cluster  $T$  measurements coming from different X-ray telescopes, which are of great value for any joint cluster analysis of eROSITA, XMM-Newton, and Chandra.

The paper is organized as follows: in Sect. 2, we describe the cluster sample used in this work. In Sect. 3 we describe the data reduction and spectral analysis of the eROSITA, XMM-Newton, and Chandra data. In Sect. 4 we describe the statistical methods followed to compare the results across different telescopes and quantify the significance of any differences. In Sect. 5, we

<sup>1</sup> We should note here that  $T$  is not used for the primary cosmological constraints of the eROSITA survey (Ghirardini et al. 2023, submitted.)

<sup>2</sup> Here we ignore the Boltzmann constant  $k_B$  multiplied by the temperature to result in energy units. Thus, we adopt the notation  $k_B T \equiv T$ .

present the cross-calibration results between all telescopes and energy bands. In Sect. 6, we present the broken power law fits for the eROSITA-Chandra scaling relations. In Sect. 7, we explore the scaling relations between the official eRASS1  $T$  values and the Chandra/XMM-Newton/spectroscopic eROSITA  $T$  values of this work. In Sect. 8, we discuss the possible reasons behind the observed  $T$  discrepancies and the impact of this work. Finally, in Sect. 9, the conclusions of this work are given.

## 2. Sample

The galaxy cluster sample used for this work was presented and described in M20. In a nutshell, it is a subsample of the eeHIFLUGCS catalog (Pacaud, et al. in prep.), which is a nearly complete, X-ray flux-limited cluster sample. eeHIFLUGCS was selected based on a re-analysis of ROSAT data of the clusters included in the Meta-Catalogue of X-ray detected Clusters of galaxies (MCXC, Piffaretti et al. 2011). After masking the Galactic plane ( $|b| \leq 20^\circ$ ) and the Magellanic clouds, the only selection criterion is an unabsorbed X-ray flux of  $f_X \geq 5 \times 10^{-12}$  ergs/s/cm<sup>2</sup> in the 0.1-2.4 keV band. Only clusters with sufficient XMM-Newton or Chandra data were kept in the M20 sample. That allowed for a precise  $T$  measurement within the  $0.2 - 0.5 R_{500}$  cluster annulus in the 0.7-7 keV band. Moreover, multiple cluster systems and clusters with strong AGN contamination were discarded. This resulted in 313 clusters in M20. In Migkas et al. (2021) we measured more properties for this sample, including the core ( $< 0.2 R_{500}$ )  $T$ , which is also utilized here. The M20  $R_{500}$  values used in this work were taken from MCXC and they were calculated through the X-ray luminosity-total mass scaling relation of Arnaud et al. (2010) for a flat  $\Lambda$ CDM cosmology with  $H_0 = 70$  km/s/Mpc and  $\Omega_m = 0.3$ . For very few clusters, the MCXC  $R_{500}$  were further corrected in M20 due to the additional cleaning of the MCXC X-ray luminosity (see M20 for details).

In this work, we use the Western Galactic hemisphere eRASS1 data to which the German eROSITA Consortium holds proprietary rights. This results in 155 different clusters from M20, which is the sample used in this work. Out of these 155, 111 are analyzed with Chandra and 53 with XMM-Newton data (with nine clusters analyzed with both instruments).

## 3. Data analysis and cluster measurements

### 3.1. eROSITA

#### 3.1.1. Data reduction

We used the first eROSITA-All Sky Survey data (eRASS:1) with processing version 010. The products of the eRASS are divided into 4,700 sky tiles, each of the size of slightly overlapping  $3.6 \times 3.6^\circ$  area (Predehl et al. 2021). We downloaded all sky tiles where the clusters of our sample are located, as well as some surrounding sky tiles for sky background estimation. The calibration and data reduction steps of the eRASS:1 data were performed with the extended Science Analysis Software (eSASS) version 211214 (Brunner et al. 2022; Merloni et al. 2024). The first step of the data reduction was to generate clean event lists and photon images. We ran the `evttool` tasks routine in the energy band  $0.2 - 10.0$  keV and set the parameters `flag=0xc00fff30` to remove bad pixels and the strongly vignetted corners of the square CCDs, and `pattern=15` to include

all patterns (single, double, triple, and quadruple). The exposure maps of the corresponding event files were generated using the `expmap` task. If multiple eRASS sky tiles were to be merged, for instance, in the case of very extended clusters, the `radec2xy` task was used to first align the sky tiles before merging them with `evttool` task. Count-rate images were generated by dividing the photon images and their corresponding exposure maps.

#### 3.1.2. eSASS Source Detection Chain

We use the eSASS source detection chain to identify and exclude point sources from the eROSITA data<sup>4</sup>. The eSASS source detection chain consists of four consecutive tasks, relying on the results already obtained during image creation. The first step is to run the `erbox` task in local mode, which is based on a sliding box algorithm and detects peaks in the image by estimating a background. It supplies a first list of possible sources in the image as well as an updated detection mask excluding the source positions (cheese map). Next, the task `erbackmap` creates a background map from an image by masking the sources found by `erbox` and smoothing. Afterward, another iteration of the task `erbox` is performed in map mode. It uses the background map to create a more accurate list of sources. Finally, the `ermlidet` task is used to characterize the sources as point or extended sources. It supplies a final source list and a source image. Additionally, the task `catprep` can be used to convert the source list into a source catalog fits file. All point and extended sources were masked with a radius large enough so the immediate surroundings of the mask converged to the local background level. There are very few cases where extended sources needed masking, due to the way the M20 sample was constructed (excluding clusters with nearby extended sources, e.g., double clusters). After the completion of the eSASS source detection chain, a visual inspection was performed to manually mask apparent sources that were missed by the algorithm.

#### 3.1.3. Spectral analysis

To extract the source and background spectra, and their Response Matrix Files (RMFs) and Ancillary Response Files (ARFs), the task `srctool` was used. We extracted spectra of all seven telescope modules combined (referred to as TM0), as well as the combinations of TM1,2,3,4,6 (TM8), and TM5,7 (TM9). The latter are the cameras affected by the optical light leak at the very soft X-ray bands (Predehl et al. 2021). To compare the results between eROSITA, XMM-Newton, and Chandra, one wants to keep the temperature measurement method as similar as possible. For this purpose, we use the exact same spectra extraction regions for the clusters as used in M20. These are the  $0.2 - 0.5 R_{500}$  annuli centered at the X-ray emission peak as seen by XMM-Newton or Chandra, as well as the cluster core region,  $< 0.2 R_{500}$ .

For the masking, two different approaches were used; in the first case, the masking process described in Sect. 3.1.2 was followed, based solely on the eROSITA point source detection and manual masking after visual inspection. As a second approach, the same masks as in the XMM-Newton and Chandra data were used. For the eROSITA-XMM-Newton clusters, we used the exact same masks as in M20, obtained from the XMM-Newton ob-

<sup>3</sup>  $R_{500}$  refers to the cluster radius within which the average cluster density is 500x the critical density of the Universe.

<sup>4</sup> At the time this analysis was performed, the official eRASS1 point source catalog (Merloni et al. 2024) was not finalized. The detected point sources in our work largely overlap with the official eRASS1 point source catalog.

servations. For the eROSITA-Chandra clusters, we masked the same point sources as in the Chandra data, but with a 30'' radius mask to account for the larger eROSITA point spread function (PSF). The two approaches returned nearly indistinguishable temperature results for nearly all clusters. This is due to the fact that we focus on central cluster regions ( $< 0.5R_{500}$ ) with high surface brightness, where minor changes in the background treatment usually have a negligible impact. Therefore, we adopted the first approach as the default one, to better "simulate" the measurements of eROSITA temperatures that future studies will wish to convert to XMM-Newton or Chandra temperatures based on our findings. The background region of each cluster was defined based on two criteria. First, the inner radius should correspond to the  $1.6R_{500}$  of the respective cluster (as in M20) so that the background spectra do not include bright residual emission from the cluster. The outer radius is calculated such that the background area is at least four times as large as the source region. In some cases, the background spectra had very few counts. In those cases, the outer radii were scaled up so that each background spectrum is expected to contain at least 300 counts, and the source detection chain was reiterated.

The spectral fitting was performed with XSPEC (Arnaud 1996) version 12.12.0. The model can be described as

$$\text{Model} = \text{constant} \times [\text{apec}_1 + \text{phabs} \times (\text{apec}_2 + \text{powerlaw})] + \text{phabs} \times \text{apec}_3 + \text{FWC}. \quad (1)$$

The constant (arcmin<sup>2</sup>) term represents the X-ray sky background (XSB) components scaled to the areas of the source regions. The components consist of the unabsorbed thermal emission from the Local Hot Bubble (LHB;  $\text{apec}_1$ ), the absorbed Milky Way Halo (MWH;  $\text{apec}_2$ ), and the cosmic X-ray background from the unresolved sources (powerlaw). The absorption along the line of sight by the Milky Way is modeled by a phabs model and its parameter is set to the  $N_{\text{H,tot}}$  values from Willingale et al. (2013) (same as in M20). The temperatures for LHB and MWH were fixed at 0.099 and 0.225 keV respectively (McCammon et al. 2002), while the photon index of the powerlaw was fixed at 1.46 (e.g., Luo et al. 2017). The second term is for the source spectra, which is an absorbed thermal emission component ( $\text{phabs} \times \text{apec}_3$ ). The last term (FWC, i.e., filter wheel closed) describes the instrumental background, which is modeled as in Veronica et al. (2024, see that paper for details). For this, we adapted the results of the eROSITA EDR FWC<sup>5</sup> data analysis. The FWC spectra were rescaled to the observed spectra using the 7 – 9 keV band, where the instrumental background dominates. The normalizations of all FWC components were left to vary. The best-fit results were then used as starting points in the subsequent spectral fittings, where the FWC normalizations were left free to vary within the  $3\sigma$  range of the best-fits.

The spectral fitting was performed in three different bands; the 0.7 – 7.0 keV (full, same band used in M20), 0.5 – 4.0 keV (soft), and 1.5 – 7.0 keV (hard) bands<sup>6</sup>. All spectra (XSB+source) were fitted simultaneously for individual TMs for each band. Moreover, the TM8 and TM9 modules were first fitted separately. As discussed in Sect. 8.3, the  $T$  results of the two modules

agree within  $\lesssim 2\sigma$ <sup>7</sup>. Therefore, we fit simultaneously both modules, that is, we use TM0 as the default for the main analysis. Additionally, we performed all fits with the metal abundance ( $Z$ ) both fixed to the M20 value and free to vary. To determine the best-fit spectral parameters, we used C-statistics (Cash 1979), which is a more suitable estimator for Poissonian counts. The Solar metal abundance table from Asplund et al. (2009) was also used.

Finally, due to its low sensitivity at high energies ( $\gtrsim 2.5$  keV), eROSITA was unable to constrain  $T$ <sup>8</sup> for 11% (23 cluster regions) of the Chandra and 33% (21) of the XMM-Newton cluster  $T$  for the full and soft bands. For the hard band, this fraction increased to 47% (96) and 60% (56) respectively. All  $T/\sigma_T < 1$  measurements were excluded from the analysis (the negligible effects of this selection are explored in Sect. 8.5). For the eROSITA-Chandra cross-calibration, this resulted in 186 (full band), 180 (soft band), and 109 (hard band) available cluster temperatures. The median  $T/\sigma_T$  is 4.4, 4.2, and 2.3 respectively. For the eROSITA-XMM-Newton cross-calibration, this resulted in 71 (full band), 68 (soft band), and 38 (hard band) cluster temperatures. The median  $T/\sigma_T$  is 3.2, 3.0, and 1.9 respectively.

## 3.2. Chandra and XMM-Newton

### 3.2.1. Data reduction

The data reduction and analysis of the Chandra and XMM-Newton observations are described in detail in Schellenberger & Reiprich (2017a) and Ramos-Ceja et al. (2019) respectively. For Chandra the ACIS I/S instruments were used, with no grating (no HETG/LETG). For XMM-Newton, the EPIC (MOS1/MOS2/PN) instrument was used. In short, pointed observations of both Chandra and XMM-Newton were treated for solar flare contamination, bad pixels, anomalous CCD state (for XMM-Newton only, Kuntz & Snowden 2008) and out-of-time events, masking of point sources and extended emission sources not related to the cluster, vignetting, exposure time correction, and instrumental background. The HEASOFT 6.20, XMMSAS v16.0.0, and CIAO v4.8 with CALDB 4.7.6 software packages were used in the M20 analysis and the full band results. Any additional spectral fitting in this work was performed using the already available spectra from M20, produced by the same software packages. For the additional soft and hard band XMM-Newton spectral analysis, we use the same software packages. For the additional Chandra spectral fitting, the CIAO v4.13 software package was used with CALDB 4.9.4.<sup>9</sup>

<sup>7</sup> For the TM9 modules that suffer from the light leak, the  $T$  estimation was rather insensitive on the exact lower energy limit that was adopted (0.7 or 0.8 keV). Thus, the same energy bands with TM8 were used.

<sup>8</sup> This means the symmetrized  $T$  uncertainty  $(\sigma_{T+} + \sigma_{T-})/2$  is larger than the best-fit  $T$  value (i.e.,  $T/\sigma_T < 1$ ), the spectral fit failed to converge, or the returned  $T$  were irrational ( $> 25$  keV or negative values).

<sup>9</sup> The full band  $T_{\text{Chandra}}$  fits were repeated with CIAO v4.13 and insignificant, non-systematic  $T$  changes were found compared to the default M20 values. Moreover, several XMM-Newton clusters were reanalyzed with HEASOFT 6.29 and XMMSAS v18.0.0. and again, no significant, systematic changes were found in the measured  $T$ . Any small  $T$  changes were significantly smaller than the scatter of the scaling relations in Sect. 5. Hence, the exact used software package versions do not affect the results and conclusions of this work.

<sup>5</sup> <https://erosita.mpe.mpg.de/edr/eROSITAObservations/EDRFWC/>

<sup>6</sup> Due to the limited number of counts, the soft and hard bands inevitably overlap between 1.5 – 4 keV. Restricting the range of either of these bands significantly reduces the quality of  $T_{\text{eROSITA}}$  constraints and the value of the cross-instrument comparison. For instance, by using the 2-7 keV band we reduce the number of available  $T_{\text{eROSITA}}$  by  $\sim 40\%$  compared to the 1.5-7 keV band.



### 3.2.2. Spectral analysis

The spectral analysis methodology for both Chandra and XMM-Newton is described in M20. In brief, we extracted two independent spectra per cluster, from within the  $\leq 0.2 R_{500}$  and  $0.2 - 0.5 R_{500}$  regions. For Chandra, the particle-induced background (PIB) was obtained from the stow event files (Schellenberger & Reiprich 2017a). It was renormalized to the 9.5-12 keV count-rate of the cluster observation before being subtracted from the source spectra. The XSB was extracted from within  $1^\circ - 2^\circ$  around the cluster using the seven ROSAT All-Sky Survey (RASS) bands (Snowden et al. 1997), as done during the M20 measurements. For XMM-Newton, the PIB was measured utilizing filter wheel closed observations. It was then rescaled to the cluster observation count-rates of the unexposed EPIC corners using the 2.5 – 5 keV (MOS and PN) and 8 – 9 keV (PN) energy bands. The XSB was extracted from the XMM-Newton field of view (FOV), from regions at  $1.6 \times \geq R_{500}$  from the cluster's center. When this was not possible, the XSB was extracted from the outer  $1'$  width annulus of the FOV. In this case, an extra, free-to-vary *apex* component was added to the XSB model to account for residual cluster emission.

The fitted model is the same as for eROSITA (Sect. 3.1.3), without the PIB component. For both Chandra and XMM-Newton, the rescaled PIB was subtracted from the source spectra. To account for an imperfect PIB subtraction, additional Gaussian lines are added to the model, representing fluorescence line residuals (for details see Schellenberger & Reiprich 2017a; Ramos-Ceja et al. 2019, M20). The XSB-only spectra are first fitted alone. The best-fit XSB values are then used as starting points and the full model (cluster emission+XSB) is left free to vary when fitting the source spectra. All properties of each model component (e.g., normalizations and temperatures) were linked across the three EPIC detectors during the XMM-Newton fits. For each spectrum, different fits are performed for three energy bands, as in eROSITA. The 0.7 – 7 keV results were taken from M20. For this work, we additionally performed the 0.5 – 4 keV and 1.5 – 7 keV spectral fits for all spectra, leaving  $Z$  free to vary and fixing  $N_H$  to the M20 value. For consistency with M20, we used XSPEC v12.9.1 for both telescopes. A  $\chi^2$ -statistic was used for both Chandra and XMM-Newton to determine the best-fit spectral parameters, as in M20<sup>10</sup>.

## 4. Statistical methodology

For the comparison of different temperature measurements, we adopt a linear relation in the logarithmic space of the form:

$$\log_{10} \frac{T_Y}{T_{\text{piv}}} = A + B \times \log_{10} \frac{T_X}{T_{\text{piv}}}, \quad (2)$$

where  $T_Y$  and  $T_X$  are the compared temperature distributions and  $A$  and  $B$  are the intercept and slope of the relation respectively. Moreover,  $T_{\text{piv}} = 4.5$  keV for eROSITA-Chandra comparisons and  $T_{\text{piv}} = 3$  keV for eROSITA-XMM-Newton comparisons (i.e., rounded median values of Chandra and XMM-Newton  $T$  distributions). Eq. 2 corresponds to a single power law in linear space. A broken (double) power law fit was also tested. However, for all temperature comparisons, it was "strongly disfavored" or "disfavored" by the Bayesian and Akaike Information

Criteria (BIC and AIC respectively), since it did not improve the fit significantly to justify the introduction of extra free parameters. Nevertheless, we present the results for a broken power law fit in Sect. 6 for the eROSITA-Chandra scaling relations, for which a broken power law fit showed the greatest improvement compared to a single power law fit.

For the linear regression of Eq. 2 we use a likelihood maximization method (LMM hereafter) as the default. Specifically, we maximize the log-likelihood function

$$\ln \mathcal{L} = -\frac{1}{2} \sum_{i=1}^N \left[ \frac{(\log T'_{Y,i} - A - B \times \log T'_{X,i})^2}{\sigma_i^2 + \sigma_{\text{intr}}^2} + \ln(\sigma_i^2 + \sigma_{\text{intr}}^2) \right] \quad (3)$$

where

$$T'_{Y,i} = \frac{T_{Y,i}}{T_{\text{piv}}}, \quad T'_{X,i} = \frac{T_{X,i}}{T_{\text{piv}}}, \quad \text{and} \quad \sigma_i^2 = \sigma_{\log T_{Y,i}}^2 + B^2 \times \sigma_{\log T_{X,i}}^2, \quad (4)$$

and  $\sigma_{\text{intr}}$  is the intrinsic scatter of the relation. Moreover,  $\sigma_{\log T} = \log e \times \frac{T_{\text{max}} - T_{\text{min}}}{2T}$  are the  $T$  measurement uncertainties in log-space, symmetrized from the (often assymmetric) linear-space 68.3%  $T$  uncertainties. The fitted parameters here are  $A$ ,  $B$ , and  $\sigma_{\text{intr}}$ . The total scatter  $\sigma_{\text{tot}}$  is given by the mean quadratic sum of  $\sigma_i$  and  $\sigma_{\text{intr}}$ .

Additionally to LMM we also utilize the Bivariate Correlated Errors and intrinsic Scatter (BCES) package by Akritas & Ber-shady (1996). For every scaling relation, the best-fit values of  $A$  and  $B$  were obtained using the BCES(orth) method. The latter minimizes the orthogonal distance of the data points compared to the best-fit line, as opposed to LMM which mostly considers the residuals on the y-axis. Due to the much larger measurement uncertainties of  $T_{\text{eROSITA}}$ , a minimization in the y-axis (as in LMM) is more appropriate than an orthogonal distance regression. Nevertheless, BCES(orth) serves as a measure of how sensitive our results are on the exact fitting method.

Similarly to Pratt et al. (2009), the total scatter in the y-axis  $\sigma_{\text{tot}}$  is measured using the error-weighted vertical distance to the best-fit regression line:

$$\sigma_{\text{tot}}^2 = \frac{1}{N-2} \sum_{i=1}^N w_i (Y_i - A_{\text{orth}} - B_{\text{orth}} \times X_i)^2 \quad (5)$$

where  $Y = \log_{10} \frac{T_{Y,i}}{T_{\text{piv}}}$  and  $X = \log_{10} \frac{T_{X,i}}{T_{\text{piv}}}$ . Furthermore,

$$w_i = \frac{1/\sigma_i^2}{(1/N) \sum_{i=1}^N 1/\sigma_i^2} \quad \text{and} \quad \sigma_i^2 = \sigma_{Y_i}^2 + B^2 \times \sigma_{X_i}^2. \quad (6)$$

$\sigma_{\text{intr}}$  is then given by the quadratic difference between  $\sigma_{\text{tot}}$  and  $\sigma_i$ . Although we use BCES(orth), we measure the scatter in the y-axis direction (instead of the orthogonal scatter) to directly compare with the results of LMM.

For both LMM and BCES, the 68.3% ( $1\sigma$ ) credible intervals of fitted model parameters are estimated by performing 10,000 bootstrap resamplings with replacement. From the posterior distribution of the best-fit parameters, we determine the 16<sup>th</sup> and 84<sup>th</sup> percentiles. In the 2-dimensional planes, the  $1$ ,  $2$ , and  $3\sigma$  ellipses are drawn by finding the ellipse with the smallest area that encompasses the 68.3%, 95%, and 99.7% of the 10,000 bootstrap data points.

<sup>10</sup> The number of counts and bins (every 25 counts) per fitted spectrum is very high (several tens of thousand counts) and the  $\chi^2$ -statistic gives very similar results to a c-statistic. The lack of significant bias due to the use of the  $\chi^2$  instead of the c-statistic is discussed in Sect. A.2.

Finally, following S15, we define a measure  $\xi$  of the statistical deviation between the two compared  $T$  distributions in linear space,

$$\xi = \text{med} \frac{T_Y - T_X}{\sqrt{\sigma_{T_Y}^2 + \sigma_{T_X}^2}}. \quad (7)$$

where the median of  $\xi$  for all clusters is considered.  $\xi$  can take both positive and negative values, depending on which  $T$  distribution is systematically higher or lower. If there is no systematic difference between the two compared instruments, one expects  $\xi \approx 0$ .

## 5. Single power law fits

All scaling relation results are shown in Table 1.

### 5.1. eROSITA vs Chandra temperatures

eROSITA returns systematically lower cluster  $T$  than Chandra for all three energy bands. The discrepancy is a function of cluster  $T$ , with hot, massive clusters deviating more than low  $T$  groups. For the latter, the two instruments seem to return similar  $T$  across all energy bands. Overall, the discrepancy between eROSITA and Chandra cluster  $T$  is the strongest for the hard energy band. This is unlike what was found in previous studies (e.g. S15, Kettula et al. 2013) where X-ray instruments tend to return consistent  $T$  in the hard band ( $> 2$  keV) while showing stronger disagreement in the soft band ( $< 2$  keV). However, the band definition in this work is different than past studies and the soft and hard bands overlap at  $1.5 - 4$  keV, therefore a direct comparison is challenging.

#### 5.1.1. Full band

The  $T$  comparison for the full band between the two instruments is displayed in the left panel of Fig. 1. The relation shows a slope of  $B = 0.781^{+0.020}_{-0.023}$ , deviating from the equality line by  $> 10\sigma$  (Fig. 2). The total scatter of the relation ( $\approx 30\%$ ) is dominated by the  $T_{\text{eROSITA}}$  uncertainties of high- $T$  clusters, rather than the intrinsic scatter ( $\approx 10\%$ ). The latter remains rather constant with increasing  $T_{\text{Chandra}}$ , only decreasing to  $\approx 5\%$  for  $T_{\text{Chandra}} \gtrsim 7$  keV, while remaining within the statistical uncertainties. Due to the energy dependence of eROSITA's effective area,  $T_{\text{eROSITA}}$  uncertainties generally increase with increasing  $T$ , which leads the total scatter to slightly increase with  $T_{\text{Chandra}}$ . Similarly, for a fixed  $T_{\text{Chandra}}$ , clusters seen as high- $T$  systems by eROSITA (i.e., upscattered) show larger uncertainties than downscattered clusters that seem to have lower  $T$ .

eROSITA returns  $\approx 25\%$  lower  $T$  than Chandra for clusters with  $T_{\text{Chandra}} = 4.5$  keV. For more massive clusters with  $T_{\text{Chandra}} = 10$  keV, the deviation rises to  $\approx 38\%$ . On the contrary, galaxy groups with  $T_{\text{Chandra}} \lesssim 2$  keV do not show any systematic  $T$  difference between the two telescopes. The value of  $\xi = -1.14$  shows that individual clusters do not deviate significantly from the equality line due to their large  $T_{\text{eROSITA}}$  uncertainties. Therefore, the large cluster sample used here is crucial to compensate for these individual uncertainties and robustly determine the cross-calibration between eROSITA and Chandra cluster  $T$ .

The single power-law fit seems to slightly overestimate the expected  $T_{\text{eROSITA}}$  for  $T_{\text{Chandra}} \approx 1$  keV clusters by  $\approx 5\%$  for LMM. Most galaxy groups at this  $T$  range seem to lie closer to the equality line. This overestimation is partially caused by a

single, upscattered cluster region (the  $0.2 - 0.5 R_{500}$  annulus of S0805). For BCES(orth), the expected  $T_{\text{eROSITA}}$  is overestimated by 18%. This strongly demonstrates that LMM provides a better fit than BCES in this case. The systematic non-gaussian scatter at low  $T$  may suggest the need for a broken power law. This is presented in Sect. 6.

#### 5.1.2. Soft band

The soft band  $T$  comparison is displayed in the middle panel of Fig. 1. The soft band  $T$  comparison is very similar to the full band one. All scaling relation parameters are consistent within  $1\sigma$  with the full band results, as shown in Fig. 2. Once again, LMM shows a steeper slope than BCES(orth), representing the low  $T$  systems better. The systematic residuals at low  $T$  persist in the soft band as well, while  $\xi$  shows that the median  $T$  discrepancy between the two instruments is only slightly larger than in the full band. Overall, no significant change is observed in the eROSITA-Chandra cross-calibration by limiting the spectroscopic analysis to softer energies.

#### 5.1.3. Hard band

The  $T$  comparison for the hard band between eROSITA and Chandra is displayed in the right panel of Fig. 1. Overall, the offset in the measured  $T$  between the two instruments is stronger in the hard band than in the soft and full bands, as shown in Fig. 2. The dependency of the offset on  $T$  is also stronger with a slope of  $B = 0.638 \pm 0.076$ ,  $1.8\sigma$  lower than in the full band. Low  $T$  systems seem consistent between the two telescopes for the hard band as well, while high- $T$  clusters deviate more than in the full and soft bands. Specifically,  $T_{\text{Chandra}} = 1$  keV clusters return the same  $T$  for both telescopes, while eROSITA measures  $\approx 44\%$  lower  $T_{\text{eROSITA}}$  for  $T_{\text{Chandra}} = 4.5$  keV systems and  $58\%$  lower  $T_{\text{eROSITA}}$  for  $T_{\text{Chandra}} = 10$  keV.  $\xi$  also has a higher value than for the other bands. The intrinsic scatter is  $\approx 3$  times larger than in the other bands and remains considerably stable for  $T_{\text{Chandra}} \lesssim 5.5$  keV. For larger  $T_{\text{Chandra}}$  it becomes similar to the values of the full and soft bands, although the statistical uncertainties are quite large to support a  $T$ -dependent scatter behavior. Finally, there is no obvious need for a broken power law in this case.

### 5.2. eROSITA vs XMM-Newton temperatures

eROSITA shows systematically lower cluster  $T$  than XMM-Newton for all three energy bands, with the discrepancy being a function of cluster  $T$ , similar to the eROSITA-Chandra comparison. However, the discrepancy is milder this time for the full and soft energy bands. For the hard band, the relation is very loosely constrained due to the large scatter. There is no obvious need for a broken power law fit for any band.

#### 5.2.1. Full band

The  $T$  comparison for the full band between eROSITA and XMM-Newton is displayed in the left panel of Fig. 3. The relation shows a slope of  $B = 0.825^{+0.074}_{-0.066}$ , supporting a  $T$ -dependence of the discrepancy between the two instruments at  $2.4\sigma$ . Considering also the intercept  $A = -0.078^{+0.016}_{-0.017}$ , which deviates more strongly from 1:1 than the slope, the overall rela-

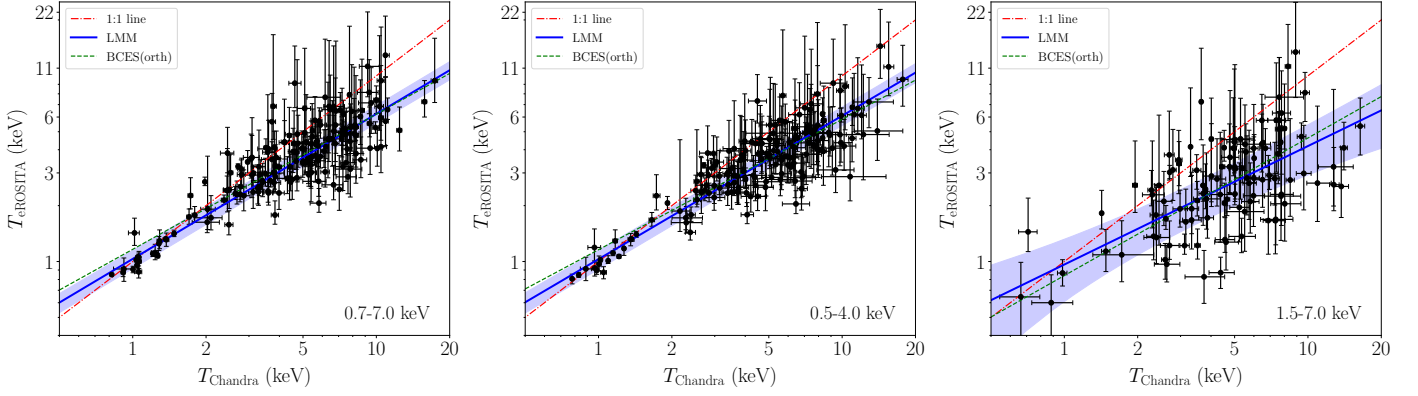


Fig. 1: Comparison between eROSITA and Chandra temperatures for the full (left), soft (middle), and hard (right) bands. The best fit scaling relation line by LMM (blue) and BCES(orth) (green dashed) are displayed. The equality 1:1 line is shown in red (dashdot). The blue shaded area represents the LMM statistical error plus the intrinsic scatter.

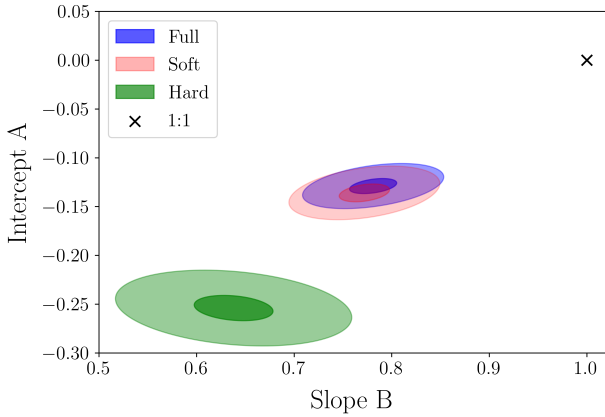


Fig. 2:  $1\sigma$  (68.3%) and  $3\sigma$  (99.7%) confidence levels for the eROSITA-Chandra scaling relations, for the full (blue), soft (pink), and hard (green) bands. The 1:1 line is represented by the black cross. The band best-fit lines for all bands deviate by  $\geq 10\sigma$  from the 1:1 line.

tion deviates from the equality line by  $\approx 5\sigma$  (Fig. 4)<sup>11</sup>, where the bulk of the tension comes from the intercept  $A = -0.078^{+0.016}_{-0.017}$ . The intrinsic scatter is once again low ( $\approx 9\%$ ) and relatively constant for  $T_{\text{XMM}} \lesssim 3.8$  keV clusters. For hotter systems, it decreases to half, but remains within the uncertainties. The total scatter is dominated by the  $T_{\text{eROSITA}}$  uncertainties.

For galaxy groups with  $T \lesssim 1.5$  keV, the two instruments agree within 5.5%. For average-sized clusters with  $T_{\text{XMM}} = 3$  keV, eROSITA measures  $\approx 16\%$  lower  $T$  than XMM-Newton. For more massive clusters with  $T_{\text{XMM}} = 7$  keV, the deviation rises to  $\approx 28\%$ . The value of  $\xi = -0.41$  is mostly affected by the clusters with  $T_{\text{eROSITA}} \geq T_{\text{XMM}}$ , which are the ones with large  $T_{\text{eROSITA}}$  uncertainties and not much statistical weight.

### 5.2.2. Soft band

The eROSITA-XMM-Newton cross-calibration in the soft band is shown in the middle panel of Fig. 3. In general, the soft band

is slightly closer to the equality line than the full band (Fig. 4), although the two bands give consistent results within  $1\sigma$ . The slightly better agreement is also shown from the lower  $\xi = -0.25$  value. Overall, the soft band scaling relation deviates by  $4.2\sigma$  by the equality line, with the main source of tension being the intercept value  $A = -0.065^{+0.018}_{-0.019}$ , which implies that  $T_{\text{XMM}} = 3$  keV clusters show a 14% lower  $T_{\text{eROSITA}}$ . Furthermore, eROSITA measures a 23% lower  $T_{\text{eROSITA}}$  for  $T_{\text{XMM}} = 7$  keV clusters, while at low- $T$  there is no meaningful difference with the full band, with the two instruments agreeing with each other. As in the eROSITA-Chandra cross-calibration, LMM fitting returns a steeper slope than BCES(orth), representing the low  $T$  systems better. Overall, a marginally better agreement between eROSITA and XMM-Newton is observed in softer X-ray energies than in the full band.

### 5.2.3. Hard band

The  $T$  comparison for the hard band between eROSITA and XMM-Newton is displayed in the right panel of Fig. 3. Due to the limited number of available  $T_{\text{eROSITA}}$  in the hard band, and their large uncertainties, the relation is not as robustly constrained as for the other bands. This is also clear from the large slope difference that LMM and BCES(orth) return. Nevertheless, one can safely conclude that eROSITA measures much lower  $T$  than XMM-Newton in the hard band. The average  $T_{\text{eROSITA}}$  underestimation for a  $T_{\text{XMM}} = 3$  keV cluster is 55%. The slope is flatter (but highly uncertain) while the intrinsic scatter is  $\approx 1.5$ –2 times larger than the respective full and soft band values. The intrinsic scatter remains stable until  $T_{\text{XMM}} \lesssim 4$  keV, while it decreases to almost zero (still within the large uncertainties however) for hotter clusters. We need to note that two strong outliers were excluded before we constrain the scaling relation, despite fulfilling the criteria for being in the sample. More details can be found in Sect. A.3.

## 6. Broken power law fits

From Fig. 1 and the systematic residuals at  $T \lesssim 2$  keV, it seems that the full and soft band eROSITA-Chandra  $T$  scaling relations might be better described by a broken power law at low  $T$  instead of a single power law. To explore this, we fit a broken power law

<sup>11</sup> Naively the reader might think this is not obvious from the eye test in Fig. 3. However, the clusters close to the 1:1 line are the ones with large  $T_{\text{eROSITA}}$  uncertainty, and hence, they carry lower statistical weight than clusters that show lower  $T_{\text{eROSITA}}$ .

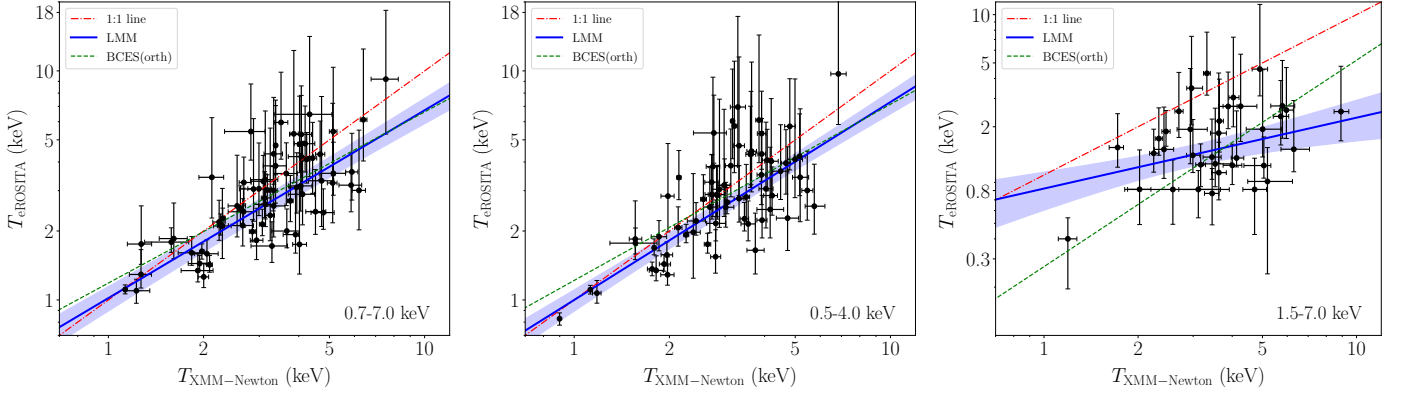


Fig. 3: Same as in Fig. 1, but for the comparison between eROSITA and XMM-Newton temperatures.

Table 1: Best-fit parameters for the eROSITA-Chandra and eROSITA-XMM-Newton scaling relations, for all energy bands and fitting methods, using the parametrization in Eq. 2 and Eq. 5.

Comparison	Band	Method	$A$	$B$	$\sigma_{\text{intr}}$	$\sigma_{\text{tot}}$	$\xi$
eROSITA-Chandra	Full	LMM	$-0.129^{+0.008}_{-0.007}$	$0.781^{+0.020}_{-0.023}$	$0.046 \pm 0.015$	$0.129 \pm 0.008$	-1.14
		BCES(orth)	$-0.112^{+0.009}_{-0.008}$	$0.728^{+0.026}_{-0.029}$	$0.040 \pm 0.006$	$0.116 \pm 0.007$	
	Soft	LMM	$-0.136 \pm 0.008$	$0.772 \pm 0.025$	$0.048 \pm 0.018$	$0.131 \pm 0.011$	-1.27
		BCES(orth)	$-0.131 \pm 0.009$	$0.702^{+0.027}_{-0.030}$	$0.041 \pm 0.006$	$0.114 \pm 0.006$	
	Hard	LMM	$-0.254 \pm 0.021$	$0.638 \pm 0.076$	$0.143 \pm 0.024$	$0.271 \pm 0.015$	-1.68
		BCES(orth)	$-0.245 \pm 0.038$	$0.741^{+0.184}_{-0.151}$	$0.095 \pm 0.012$	$0.231^{+0.012}_{-0.016}$	
eROSITA-XMM-Newton	Full	LMM	$-0.078^{+0.016}_{-0.017}$	$0.825^{+0.074}_{-0.066}$	$0.038 \pm 0.019$	$0.164 \pm 0.013$	-0.41
		BCES(orth)	$-0.047 \pm 0.017$	$0.747^{+0.082}_{-0.094}$	$0.067 \pm 0.007$	$0.144 \pm 0.009$	
	Soft	LMM	$-0.065^{+0.018}_{-0.019}$	$0.869^{+0.073}_{-0.067}$	$0.027 \pm 0.016$	$0.174 \pm 0.014$	-0.25
		BCES(orth)	$-0.025 \pm 0.020$	$0.769^{+0.094}_{-0.116}$	$0.074 \pm 0.009$	$0.156 \pm 0.011$	
	Hard	LMM	$-0.351^{+0.038}_{-0.036}$	$0.442^{+0.205}_{-0.182}$	$0.055 \pm 0.039$	$0.263 \pm 0.024$	-2.31
		BCES(orth)	$-0.434^{+0.043}_{-0.041}$	$1.287^{+0.698}_{-0.400}$	$0.107 \pm 0.041$	$0.279 \pm 0.033$	

$$\log_{10}\left(\frac{T_Y}{T_{\text{piv}}}\right) = A_{\text{bpl}} + \begin{cases} B_1 \times \log_{10}\left(\frac{T_X}{T_{\text{break}}}\right), & \text{for } T_X \leq T_{\text{break}} \\ B_2 \times \log_{10}\left(\frac{T_X}{T_{\text{break}}}\right), & \text{for } T_X > T_{\text{break}}. \end{cases} \quad (8)$$

where  $T_{\text{break}}$  is the  $T$  where the power law changes (the so-called power law "knee") and  $B_1$  and  $B_2$  are the slopes of the power laws before and after  $T_{\text{break}}$ . Notice that the intercept  $A_{\text{bpl}}$  here corresponds to  $T_{\text{break}}$  and not  $T_{\text{piv}}$  as in the single power law case. Therefore,  $A$  and  $A_{\text{bpl}}$  should not be compared. Moreover, the two power law parts have their own  $\sigma_{\text{intr}}$  fitted. The fitting is performed only with LMM, since BCES(orth) does not allow for a broken power law fit. Finally, the  $T_{\text{break}}$  uncertainty is rather large and degenerates the fit of all other parameters as well, mak-

ing the fit non-informative. Therefore, we fix  $T_{\text{break}}$  to its best-fit value.

We stress again that both the BIC and AIC criteria disfavor the broken power law compared to the single power law fit. This is because the improvement of the fit (i.e., an increase of model likelihood  $\ln \mathcal{L}$ ) is not enough to justify the extra, fitted model parameters<sup>12</sup>. Nevertheless, this is probably due to the limited number of low- $T$  clusters to which the first part of the broken power law is fitted and not due to the lack of a real break in the scaling relation. Therefore, the broken power law results might be more accurate for converting eROSITA and Chandra  $T$  in the full and soft band (i.e., reduced scatter compared to single power law), even if this is not strictly justified from BIC and AIC. Finally, all broken power law scaling relation results are shown in Table 2.

<sup>12</sup> This conclusion does not change even if we use a single  $\sigma_{\text{intr}}$  parameter for the broken power law



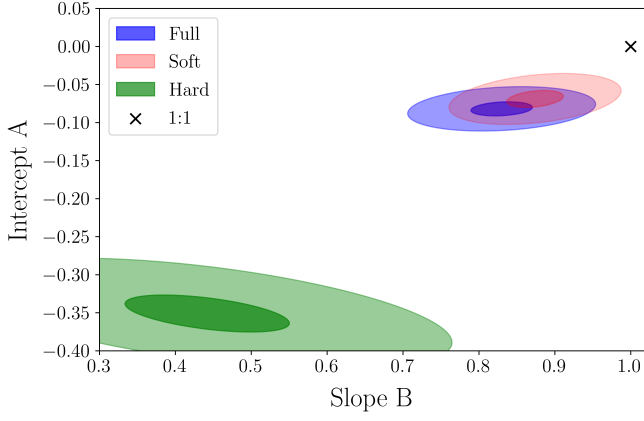


Fig. 4:  $1\sigma$  (68.3%) and  $3\sigma$  (99.7%) confidence levels for the eROSITA-XMM-Newton scaling relations, for the full (blue), soft (pink), and hard (green) bands. The 1:1 line is represented by the black cross. The full and soft band best-fit lines deviate by  $5\sigma$  and  $4.2\sigma$  respectively from the 1:1 line.

### 6.1. Full band

The fit results for eROSITA-Chandra full band comparison are shown in the top panel of Fig. 5. The break in the power law is detected at 2.7 keV, where eROSITA measures 7% lower  $T$  than Chandra. For lower  $T$ , the slope is  $B_1 = 0.946 \pm 0.022$ , very close to unity. Combined with the intercept  $A_{\text{bpl}} = -0.031 \pm 0.008$ , one sees that the low- $T$  part is similar to the 1:1 line as  $T$  decreases, although the statistical deviation from the equality line is still  $\approx 4\sigma$ . More specifically, eROSITA shows only  $\approx 2-5\%$  lower  $T$  for  $T_{\text{Chandra}} \approx 1-2$  keV clusters, lower than typical measurement uncertainties. The intrinsic scatter is also very small; 3.7% for  $T \leq 2.7$  keV, consistent with zero at  $2\sigma$ .

For  $T > 2.7$  keV the slope  $B_2 = 0.614 \pm 0.024$ , strongly demonstrating the more highly evolving discrepancy between the two instruments as  $T$  increases.  $B_2$  is 24% flatter than the single power law slope and 43% lower than  $B_1$ . The intrinsic scatter is  $\approx 2.8$  times larger than the respective low- $T$  value, at 10%. Overall, the broken power law fit brings closer the two instruments in terms of measured  $T$  compared to the single power law fit for  $T \leq 5.3$  keV clusters, while it increases their discrepancy for  $T > 5.3$  keV systems.

### 6.2. Soft band

The soft band fit results for the eROSITA-Chandra comparison are displayed in the bottom panel of Fig. 5. The break in the power law is detected at 1.7 keV. For  $T \leq 1.7$  keV,  $T_{\text{eROSITA}}$  and  $T_{\text{Chandra}}$  are consistent within  $\leq 2.5\%$ . The low- $T$  scaling relation with  $B_1 = 0.979 \pm 0.042$  and  $A_{\text{bpl}} = -0.011 \pm 0.009$  is consistent with the 1:1 line at only  $\approx 1\sigma$ , closer than the full band fit. The intrinsic scatter is again small and relatively consistent with zero. Thus, no significant deviation from the 1:1 line is observed at the soft band for low- $T$  clusters.

For  $T > 1.7$  keV, the relation deviates from 1:1 as  $T$  rises, with  $B_2 = 0.700 \pm 0.019$ . However, it returns a less discrepant result than the full band broken power law at high  $T$ . The intrinsic scatter is  $> 3$  times larger than the respective low- $T$  value, at 13%. Compared to the single power law fit, the broken power law brings closer the measured  $T$  of the two instruments at  $T \leq 4.3$  keV, while it increases their tension for  $T > 4.3$  keV clusters.

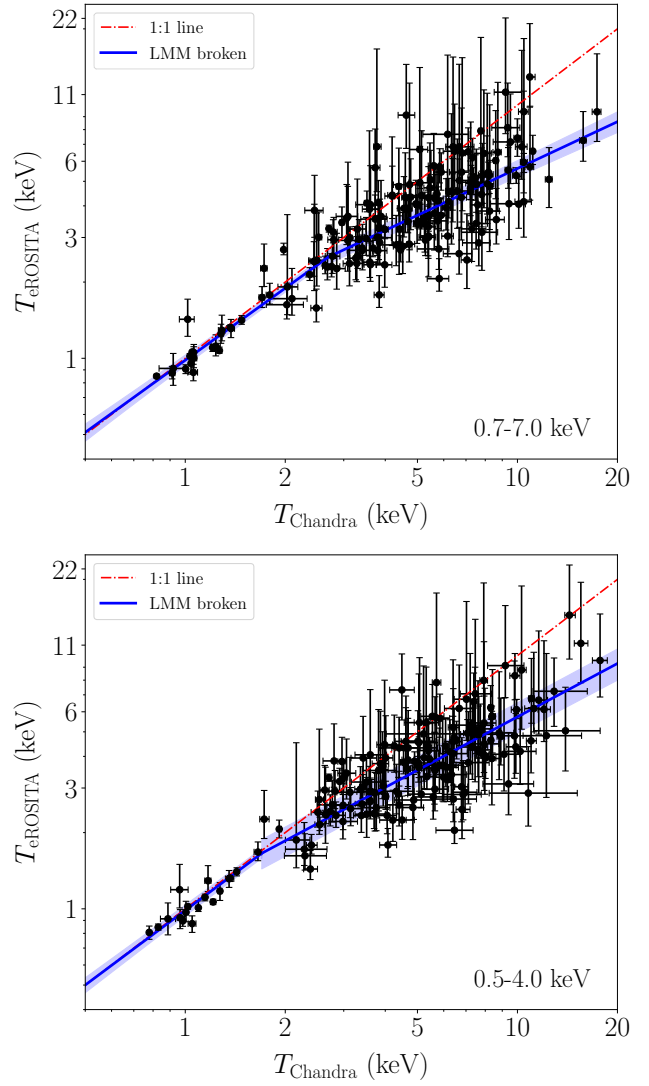


Fig. 5: Same as in Fig. 1, but with a broken power law fitted with LMM for the full (top) and soft (bottom) bands, as shown in Eq. 8. The break point of the power law is found at  $T_{\text{break}} = 2.7$  keV and 1.7 keV respectively. The low- $T$  clusters are much better fitted than the single power law fit, showing consistency between instruments. At high- $T$ , the best-fit line deviates more from the 1:1 line than the single power law fit.

## 7. eRASS1 cluster catalog $T$ vs Chandra, XMM-Newton, and spectroscopic eROSITA $T$

The eRASS1 galaxy cluster catalog (Bulbul et al. 2024) includes cluster  $T$  measurement determined by the MultiBand Projector 2D (MBProj2D) software<sup>13</sup> (Sanders et al. 2018). MBProj2D is a tool that uses X-ray images of galaxy clusters in different, independent energy bands, and through forward-modeling, constrains X-ray cluster properties such as the surface brightness and temperature profiles. The cluster  $T$  provided in the eRASS1 galaxy cluster catalog is constrained using seven independent energy bands between 0.3-7.0 keV and within the entire  $R_{500}$  of the cluster (for more details see Bulbul et al. 2024).

In order to provide conversion functions between the eRASS1 cluster catalog  $T$  and equivalent spectroscopic  $T$  from

<sup>13</sup> <https://github.com/jeremysanders/mbproj2d>

Table 2: Best-fit parameters for the eROSITA-Chandra broken power law scaling relations in the full and soft bands, using the LMM method and the parametrization in Eq. 8.

$T$ range	$A$	$B$	$\sigma_{\text{intr}}$	$\sigma_{\text{tot}}$
Full band				
$T_{\text{Chandra}} \leq 2.7 \text{ keV}$	$-0.031 \pm 0.008$	$0.946 \pm 0.022$	$0.016 \pm 0.008$	$0.062 \pm 0.009$
$T_{\text{Chandra}} > 2.7 \text{ keV}$		$0.614 \pm 0.024$	$0.045 \pm 0.017$	$0.151 \pm 0.008$
Soft band				
$T_{\text{Chandra}} \leq 1.7 \text{ keV}$	$-0.011 \pm 0.009$	$0.979 \pm 0.042$	$0.017 \pm 0.008$	$0.041 \pm 0.006$
$T_{\text{Chandra}} > 1.7 \text{ keV}$		$0.700 \pm 0.019$	$0.057 \pm 0.018$	$0.162 \pm 0.011$

Chandra, XMM-Newton, and eROSITA, we study the scaling relations between these different measurements. It is *crucial* to stress here that this comparison does not serve as a cross-calibration test between eROSITA and other instruments. In these comparisons, the cluster area used, the methodology (MBproj2D  $T$  vs spectroscopic  $T$ ), and the energy bands used for the eRASS1 and Chandra/XMM-Newton  $T$  are all different. Therefore, the sole purpose of this comparison is to constrain the conversion functions between different types of  $T$ . Since the eRASS1  $T$  refers to the entire  $R_{500}$ , we can only compare with a single  $T$  per cluster for Chandra, XMM-Newton, and spectroscopic eROSITA; that is, with core-only or annulus-only  $T$ . Finally, the comparisons are presented only for the full band.

We matched all the clusters from M20 with all the eRASS1 cluster catalog systems that have available  $T$  measurements. Since  $z$  correlates with  $T$  during spectral fittings, we excluded six clusters that showed a redshift difference of  $\left| \frac{\Delta z}{1 + z_{\text{M20}}} \right| > 0.01$ <sup>14</sup> between M20 and the eRASS1 cluster catalog. This resulted in 78 eRASS1-Chandra, 33 eRASS1-XMM-Newton, and 96 eRASS1-spectroscopic eROSITA clusters.

The best-fit scaling relation parameters for the  $T$  comparison between the eRASS1 cluster catalog and the other spectroscopic  $T$  measurements are presented in Table 3.

### 7.1. eRASS1 vs Chandra temperatures

The eRASS1 vs Chandra  $T$  comparison is displayed in the left panel of Fig. 6. Both the core and core-excised  $T_{\text{Chandra}}$  show similar deviations from  $T_{\text{eRASS1}}$ . The main difference is found in the negligible intrinsic scatter of the relation when the core  $T_{\text{Chandra}}$  is used.  $T_{\text{eRASS1}}$ , which come from the full  $R_{500}$  area of the clusters, are expected to be mostly influenced by the cluster core, since this is where most of the emission originates. The eRASS1-Chandra scaling relations agree slightly better than the results presented in Sect. 5.1, but within the statistical uncertainties. The eRASS1-Chandra relations still deviate from the equality line by  $> 10\sigma$ .  $T_{\text{eRASS1}}$  are 22% (21%) lower than the core-excised (core)  $T_{\text{Chandra}}$  for  $T_{\text{Chandra}} = 4.5$  keV. For hotter plasma with  $T_{\text{Chandra}} = 10$  keV, the deviation rises to 32% (28%). Cooler gas values of  $T_{\text{Chandra}} = 2$  keV disagree by 10% (21%) between the eRASS1 catalog and Chandra. However, these differences come with non-negligible uncertainties and individual clusters

can deviate significantly from these averages. Overall, the conclusions from the eRASS1-Chandra  $T$  comparisons do not significantly change compared to the results presented in Sect. 5.1.

### 7.2. eRASS1 vs XMM-Newton temperatures

The eRASS1 vs XMM-Newton  $T$  comparison is displayed in the middle panel of Fig. 6. Due to the limited sample and the significant scatter, no statistical significant differences can be found between the core and core-excised  $T_{\text{XMM}}$  compared to  $T_{\text{eRASS1}}$ , although the core-excised  $T_{\text{XMM}}$  offers a best-fit relation slightly closer to the equality line. The eRASS1-XMM-Newton scaling relations are consistent with the results presented in Sect. 5.2 within the uncertainties. However, the best-fit functions deviate more than the equality line compared to the comparison with the spectroscopic  $T_{\text{eROSITA}}$  in 5.2, while the scatter here is also larger. For cool gas with  $T_{\text{XMM}} = 1.5$  keV,  $T_{\text{eRASS1}}$  is found within 2% (13%) when the core-excised (core) scaling relation is considered. Respectively, for  $T_{\text{XMM}} = 3$  keV the difference is 18% (23%), while it rises to 34% (33%) for  $T_{\text{XMM}} = 7$  keV.

### 7.3. eRASS1 vs spectroscopic eROSITA temperatures

The comparison between the eRASS1 and the spectroscopic eROSITA  $T$  measured in this work is displayed in the right panel of Fig. 6. Both the core-excised and core scaling relations show excellent agreement with the equality line (the core relation practically coincides with the 1:1 line). The scatter of the relations is almost exclusively driven by the  $T$  measurement uncertainties with no significant intrinsic scatter being present.

## 8. Discussion

The accurate characterization of the cross-calibration of different X-ray telescopes is crucial to understand the systematic biases and uncertainties of the effective area calibration of X-ray instruments. Furthermore, if the cross-calibration factor between two instruments is not well-known, it hinders the joint analysis of data sets coming from different telescopes.

In the previous sections, we used a large galaxy cluster  $T$  sample for the first time to establish that eROSITA shows systematically lower cluster  $T$  compared to Chandra and XMM-Newton. This discrepancy was found to be stronger the hotter a cluster is, with  $T \lesssim 2$  keV clusters not showing significant differences between eROSITA and the other instruments. In general, the soft energy band 0.5 – 4.0 keV showed slightly better agree-

<sup>14</sup> Alternative filtering based on a 10% or 20% redshift difference results in similar cuts and have a completely negligible effect on the analysis.

Table 3: Best-fit parameters for the eROSITA-Chandra and eROSITA-XMM-Newton scaling relations, for all energy bands and fitting methods, using the parametrization in Eq. 2 and Eq. 5.

Comparison	Cluster region	$A$	$B$	$\sigma_{\text{intr}}$	$\sigma_{\text{tot}}$	$\xi$
eRASS1-Chandra	Core-excised	$-0.107 \pm 0.012$	$0.831 \pm 0.030$	$0.037 \pm 0.010$	$0.136 \pm 0.008$	-1.03
	Core	$-0.103 \pm 0.011$	$0.880 \pm 0.024$	$0.003^{+0.007}_{-0.003}$	$0.118 \pm 0.008$	-0.95
eRASS1-XMM-Newton	Core-excised	$-0.086 \pm 0.029$	$0.738 \pm 0.088$	$0.077^{+0.041}_{-0.032}$	$0.210 \pm 0.016$	-1.45
	Core	$-0.113 \pm 0.027$	$0.823 \pm 0.113$	$0.033^{+0.039}_{-0.023}$	$0.174 \pm 0.015$	-0.45
eRASS1-eROSITA spec- $T$	Core-excised	$-0.003 \pm 0.014$	$0.934 \pm 0.049$	$0.027^{+0.017}_{-0.011}$	$0.194 \pm 0.011$	-0.05
	Core	$-0.003 \pm 0.011$	$1.004 \pm 0.026$	$0.000^{+0.002}_{-0.000}$	$0.178 \pm 0.010$	-0.01

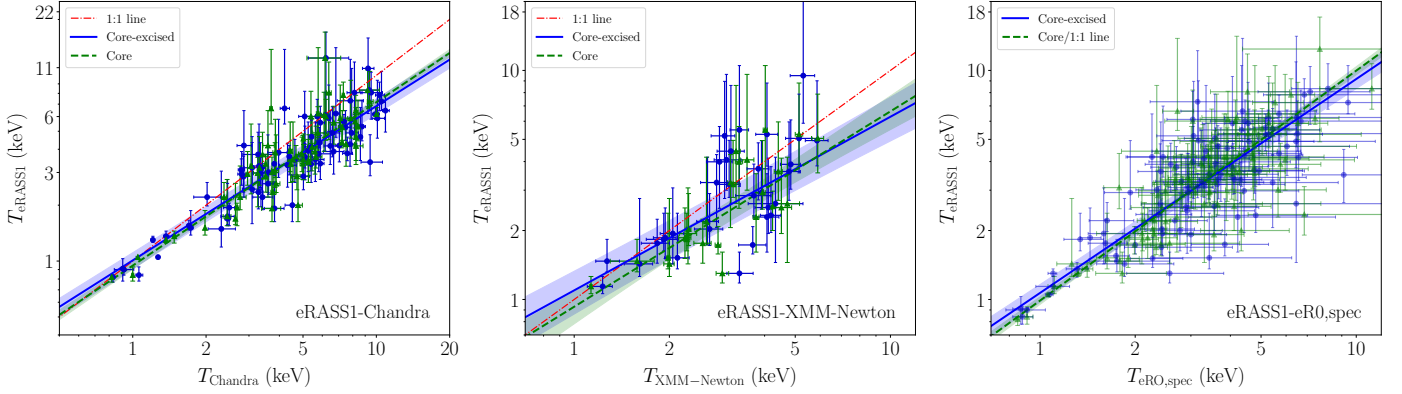


Fig. 6: Comparison between eRASS1 and Chandra (left), XMM-Newton (middle), and spectroscopic eROSITA (right) temperatures. The comparison between the core-excised (core)  $T_{\text{Chandra}}/T_{\text{XMM}}/T_{\text{eROSITA,spec}}$  and the single  $T_{\text{eRASS1}}$  from the entire  $R_{500}$  is displayed in blue (green). The best fit scaling relation lines are displayed with the same colors. The equality 1:1 line is shown in red (dashdot), except for the right panel, where it coincides with the green best-fit line. The blue and green shaded areas represent the statistical error plus the intrinsic scatter for the core-excised and core scaling relations respectively.

ment between different instruments than the full  $0.7 - 7.0$  keV band. At the same time, restricting the spectral fitting to hard X-ray energies ( $1.5 - 7.0$  keV) significantly increased the difference between  $T_{\text{eROSITA}}$  and the other  $T$  measurements. All the above indicates that the cross-calibration between eROSITA, Chandra, and XMM-Newton, is a function of spectral shape and energy range used, with the softer spectra showing better agreement.

Opposite to the eROSITA cross-calibration results, most past studies found that the cluster  $T$  differences between other X-ray instruments seem to be stronger at soft X-ray energies and more consistent at harder X-ray bands. In general, these studies failed to pinpoint a specific systematic causing these cross-calibration differences, although a wide range of possible causes was investigated (e.g., S15). The observed cluster  $T$  differences were attributed to systematic effective area calibration uncertainties. In this section, we discuss and examine the possible systematic biases behind the established discrepancy between eROSITA  $T$  with Chandra and XMM-Newton  $T$ .

### 8.1. Metal abundance degeneracy with temperature

The determination of  $T$  through spectral fitting is partially influenced by the (mildly) correlated metal abundance  $Z$ . When converting  $T$  values between different X-ray instruments, accounting for the unknown  $Z$  value of the second instrument is

not feasible; thus one assumes the  $Z$  from the first instrument. For this reason, we adopted the  $Z$  values from Chandra and XMM-Newton measurements to use during the eROSITA spectral fitting. However, since the best-fit  $T$  and  $Z$  values are correlated, fixing  $Z$  could potentially bias the  $T_{\text{eROSITA}}$  values. In other words, if eROSITA measured systematically different  $Z$  and consistent  $T$  values, fixing  $Z$  might erroneously interpret this as a  $T$  discrepancy. Furthermore, due to the so-called "Fe bias" (e.g., Buote 2002; Mernier et al. 2018; Riva et al. 2022), forcing  $Z$  to be the same between instruments with different soft- and hard-band sensitivity ratios (e.g., eROSITA and Chandra) might lead to systematic  $T$  discrepancies if multiphase gas is present. To test if fixing eROSITA  $Z$  to the Chandra and XMM-Newton values causes a systematic bias, we repeated the entire analysis, this time leaving  $Z$  free to vary during the eROSITA spectral fits.

The best-fit results can be found in Table A.1. No scaling relation changes significantly when the new  $T_{\text{eROSITA}}$  are used. In fact, the full and soft band scaling relations for both Chandra and XMM-Newton shift further from the 1:1 line for  $T \gtrsim 3$  keV clusters, while the low- $T$  end maintains the relative consistency that showed for the fixed  $Z$  case. In general, the best-fit  $A$  and  $B$  slightly decrease by a few percent, while the scatter increases. The hard band is the most insensitive one to the varying  $Z$  change. To conclude, the discrepancy between eROSITA and other telescopes remains the same or increases for all com-

parisons when  $Z$  is left free to vary, disproving the treatment of  $Z$  as the cause of the discrepancy. This is consistent with S15, who also did not find a significant improvement in the Chandra-XMM-Newton cross-calibration when using the same or different  $Z$  for the two telescopes.

## 8.2. Different soft/hard X-ray sensitivities of effective areas

### 8.2.1. Multitemperature gas structure

The intracluster medium has a multitemperature structure, which is typically a function of the distance from the cluster center. The observed spectra we use come from 2-dimensional cluster circles and annuli, which include the projection of outer cluster regions in the same line of sight. Hence, the observed spectra include several  $T$  gas components which are eventually fitted by a single- $T$  model. In addition, multiphase gas might be present at the same cluster radius (e.g. cold and hot gas clouds). In both of these cases, the different sensitivity of the eROSITA effective area at different energies compared to Chandra and XMM-Newton could result in a systematic bias in the measured single- $T$ . As shown in Fig. 7, eROSITA's effective area drops more rapidly from soft to hard X-ray energies compared to Chandra and XMM-Newton. Consequently, it will potentially assign more weight to the low- $T$  components of multiphase cluster gas, leading to systematically lower measured single- $T$  than the other two telescopes. Such a discrepancy could be also enhanced due to the Fe bias. The latter tends to underestimate single- $T$  measurements when multiphase gas is present, with the effect being stronger for instruments more sensitive to the soft band. The bias introduced to single- $T$  fits due to multiphase gas was discussed in detail in several past studies (e.g., Reiprich et al. 2013). In past cross-calibration studies, this was disfavored as the reason behind the observed calibration discrepancy between XMM-Newton and Chandra (e.g., S15) and other instruments. Nevertheless, it is important to also test this for the eROSITA calibration to fully understand the importance of this possible systematic.

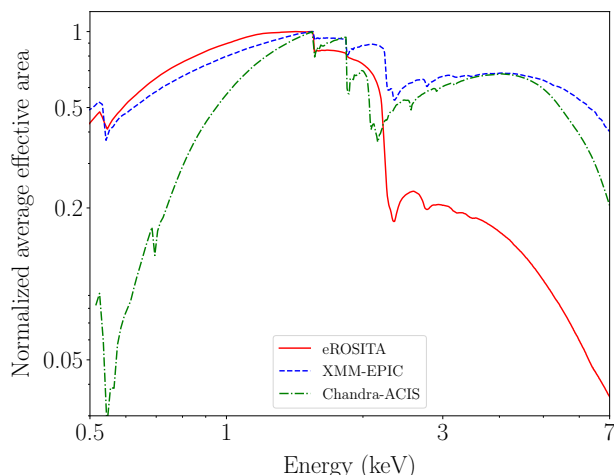


Fig. 7: Normalized average effective area for eROSITA TM0 (red, solid), XMM-Newton-EPIC (blue, dashed), and Chandra-ACIS (green, dot dashed), as derived from the spectra used in this work.

**Observational test** To do so, firstly we divide our sample into two subsamples; cluster core  $T$  and cluster annulus  $T$ . The former are expected to show stronger discrepancies between eROSITA and the other instruments. This is due to a higher level of multitemperature structure in the core spectra caused by projection effects and the presence of the (often complicated) cluster core. The comparisons are performed in the full band since the broader band is expected to be more affected by the soft-hard ratio differences of the instruments' effective areas. The  $T$  distributions of the two subsamples are very similar (see Fig. A.2).

Comparing the  $T$  cross-calibration scaling relations for core and annulus spectra, one sees there are no statistically significant differences. As shown in the top panel of Fig. 8, the core vs annulus scaling relations deviate by  $\lesssim 1\sigma$  for both the eROSITA-Chandra and eROSITA-XMM-Newton comparisons. Interestingly, the core  $T$  scaling relations for both instruments are slightly shifted towards the 1:1 line (still significantly far away though) despite their more intense bias by the multiphase cluster gas. One would need more data to better understand if this shift is a statistical fluctuation or a true effect.

**Simulations from past studies** Moreover, ZuHone et al. (2023) used hydrodynamical simulations to assess the bias that multitemperature structure that resembles realistic cluster temperature profiles, introduces to single- $T$  fits of eROSITA. They found that spectroscopic, single thermal models underestimate  $T$  by  $\sim 10 - 15\%$  compared to the mass-weighted simulated  $T$ , with no strong  $T$  dependence of this discrepancy. This underestimation is not enough to explain the observed  $T$  differences between eROSITA and the other telescopes. On the other hand, compared to the X-ray emission-weighted simulated  $T$ , ZuHone et al. (2023) found that a spectroscopic, single thermal model underestimates  $T$  by  $\sim 25 - 30\%$ . If there was no such bias for Chandra and XMM-Newton  $T$ , this discrepancy would be enough to alleviate most of the tension between  $T_{\text{eROSITA}}$  and the rest. However, both Chandra and XMM-Newton, are expected to also return underestimated  $T$  from single thermal fits, but likely at a lesser degree. Until a similar analysis is performed for these two X-ray instruments, it is unclear exactly how the  $T$  comparison between them and eROSITA would be affected.

A relevant test was performed by Reiprich et al. (2013) where they fit a single- $T$  model to a two-temperature simulated gas with a hot ( $T_{\text{hot}} = 8$  keV) and a cold ( $T_{\text{cold}} = 0.5$  keV) component. They found that Chandra, XMM-Newton, and eROSITA are all expected to return a best-fit  $T$  lying between of the two  $T$  components, but eROSITA returns the lowest  $T$ . The reported discrepancy is similar to the  $T$  differences we observe in this work. However, to illustrate the effect, Reiprich et al. (2013) used extreme  $T$  differences that are not present in the data we used, where the expected differences, given the measured core and core-excised  $T$  and typical cluster  $T$  profiles, are much smaller. Also, as noted in S15, such extreme  $T$  differences of a two-phase plasma would result in high reduced chi-square values from the single- $T$  fits; this is not observed in our spectral fits. Finally, in that case one would also expect the eROSITA-Chandra core- $T$  comparison to deviate more than the annulus- $T$  comparison, which is not the case (Fig. 8).

**Simulations in this work** To test the effects of multitemperature structure on eROSITA  $T$  more extensively, we used XSPEC to simulate multitemperature plasma spectra, following the same approach as in Reiprich et al. (2013) and S15. We simulated spectra with two temperature components and fit them with a



single temperature model, as for the real data. We used  $T_{\text{cold}} = 0.5, 0.75, 1$  keV and  $T_{\text{hot}} = 1, 2, 4, 6$  keV, covering a wide and realistic range of  $T$  combinations. The redshift and metallicity were kept fixed to  $z = 0.05$  and  $Z = 0.3 Z_{\odot}$  respectively, which are typical values for the cluster sample we use. Moreover, we used four emission measure ratios (EM) between the cold and hot  $T$  components, EM= 0.01, 0.05, 0.10, 0.15 (as explained later, higher EM returned unrealistic results). For every combination, we simulated 125 random spectra, with a typical number of counts for every instrument, based on the real spectra. In total, we simulated and fitted 6000 spectra with a single  $T$  model for eROSITA (TM0), XMM-Newton (combined EPIC and PN-only), and Chandra (ACIS). We assumed that the calibration of each instrument is perfect and, consequently, any differences between instruments should originate due to their different energy dependence of their effective areas.

The average results for the full band eROSITA-Chandra and eROSITA-XMM-Newton comparisons are displayed in Fig. 9. It is evident that the observed cross-calibration differences are unlikely to be explained due to possible  $2T$  thermal structure in the fitted spectra. although eROSITA returns slightly lower single  $T$  values than Chandra and XMM-Newton in all cases, the  $T$  difference is always  $\leq 20\%$ . The only combination for which the  $2T$  structure could mostly explain the observed  $T$  discrepancies between eROSITA and the other instruments is the most extreme case with  $T_{\text{cold}} = 0.5$  keV and EM= 0.15. However, these models on average return  $\chi^2 \sim 1.3 - 1.6$  which suggests a bad fit. Such increased  $\chi^2$  values are not generally seen in the real data. Subsequently, such cold, bright  $T$  components in the observed spectra are disfavored as the reason for the observed  $T$  discrepancy. Higher EM values return even higher  $\chi^2$  values, and as such, they are not explored further. On the other hand,  $T_{\text{cold}} = 0.5$  keV and EM= 0.10 models return  $\chi^2 \leq 1.15$ , which is rather consistent with the observed  $\chi^2$ . Such models can alleviate most (but not all) of the  $T$  tension between eROSITA-Chandra and eROSITA-XMM-Newton. All other combinations with  $T_{\text{cold}} \geq 0.75$  keV do not show significant  $T$  differences between instruments, regardless of the EM and  $T_{\text{hot}}$  values. We reach the same conclusion when we only use the PN detector of XMM-Newton to fit the spectra. Finally, we repeat the analysis using the hard band fits only. In this case, the observed cross-calibration differences cannot be explained by the  $2T$  structure in the simulated data, since eROSITA returns very similar single  $T$  results to Chandra and XMM-Newton, regardless of the exact model values. The results are presented in Sect. A.4 and Fig. A.3.

**Conclusions on multitemperature structure bias** Given all the above, the bias introduced by multiphase gas and different effective areas is currently disfavored as the main cause for the observed  $T$  discrepancy between eROSITA and Chandra/XMM-Newton. This is consistent with what past studies found for other instrument comparisons (e.g., S15). However, to accurately quantify the exact level of bias introduced due to more complicated multiphase gas structure, more work is needed.

### 8.2.2. Bias from Galactic absorption

The X-ray absorption, proxied by the  $N_{\text{H}}$  parameter, has a much stronger influence on the soft part of the spectra ( $\lesssim 1.5$  keV) than the hard part, for which it is almost irrelevant. Given the different energy-dependent shapes of the effective areas of the telescopes, different  $N_{\text{H}}$  values can affect each telescope's  $T$  measurements differently, introducing an  $N_{\text{H}}$ -dependent systematic bias in the

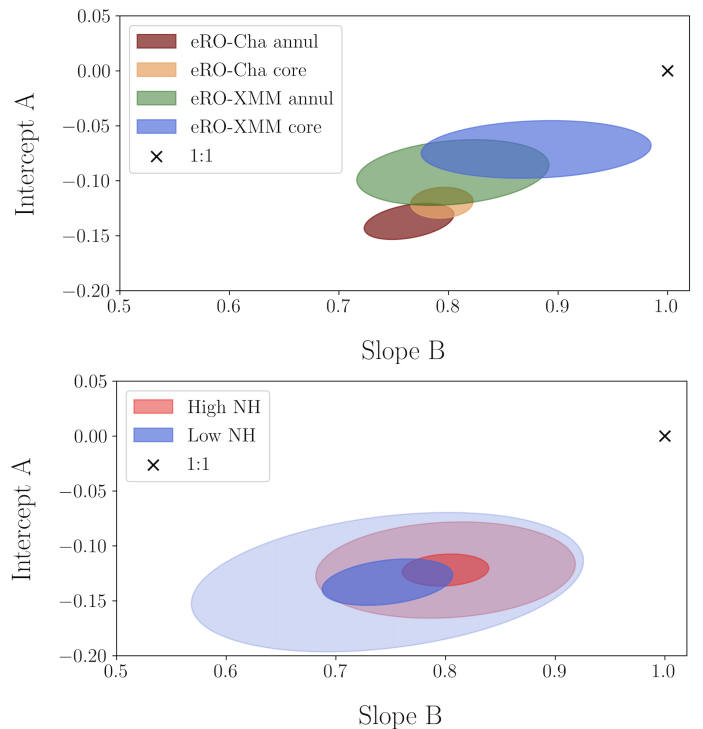


Fig. 8: *Top*:  $1\sigma$  (68.3%) confidence levels for the core-only and annulus-only eROSITA-Chandra and eROSITA-XMM-Newton scaling relations, for the full band. The colors are explained in the figure legend. The best-fit results do not differ significantly for core and annuli cluster  $T$ , for any instrument comparison. *Bottom*:  $1\sigma$  (68.3%) and  $3\sigma$  (99.7%) confidence levels for the eROSITA-Chandra scaling relations for high  $N_{\text{H}}$  (pink) and low  $N_{\text{H}}$  (blue) clusters. The contours correspond to the full band. The 1:1 line is represented by the black cross. The best-fit results are very similar between clusters with low and high Galactic absorption.

$T$  comparison for the soft and full bands (while the hard band would remain unaffected from such bias). To address this possibility, we compare the full band eROSITA-Chandra scaling relations between the  $\frac{1}{3}$  of the sample with the lowest and highest  $N_{\text{H}}$ <sup>15</sup>. The two subsamples do not show significant differences in their  $T$  distributions and any difference is expected to come from the different  $N_{\text{H}}$ .

As displayed in the bottom panel of Fig. 8, the effect different  $N_{\text{H}}$  values have on the eROSITA-Chandra cross-calibration is not statistically significant, with the low and high  $N_{\text{H}}$  subsamples agreeing within  $\lesssim 1\sigma$ . Therefore, this further supports the notion that the different effective area dependence on photon energy per telescope is not the cause of the  $T$  discrepancy.

### 8.3. Bias introduced from eROSITA TM8 vs TM9

Next, we explore the effect that the inclusion of eROSITA TM9 data has on the  $T$  measurements. As discussed in Sect. 3.1.3, TM9 cameras are affected by the light leak. In theory, this could potentially alter the signal at low X-ray energies while the harder energies remain unaffected, biasing the fitted  $T$ . This would not explain the observed  $T$  discrepancies in the hard band, but it is

<sup>15</sup> The subsamples for the eROSITA-XMM-Newton comparison are too small to return meaningfully constrained results.

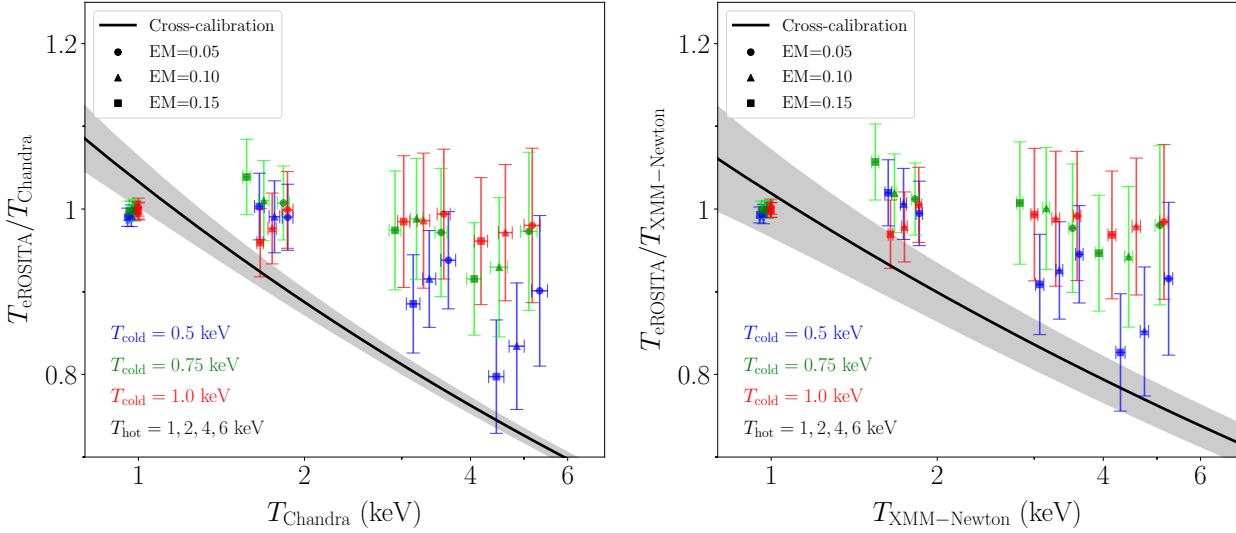


Fig. 9: Ratio of the eROSITA and Chandra (left) and eROSITA and XMM-Newton (right) single- $T$  fits to simulated spectra with two temperature components, as a function of the Chandra and XMM-Newton best-fit single- $T$  respectively. Blue, green, and red colors correspond to  $T_{\text{cold}} = 0.5, 0.75, 1$  keV respectively. The hot component has values of  $T_{\text{hot}} = 1, 2, 4, 6$  keV. The circles, triangles, and squares correspond to emission measures of  $\text{EM} = 0.05, 0.10, 0.15$  for the cold and hot components. The black curve shows the observed  $T$  difference between eROSITA-Chandra (left) and eROSITA-XMM-Newton (right) as presented in Table 1.

worth checking if it has any effect on the other bands. To test the consistency of the two telescope modules, we fit the TM9-TM8  $T$  scaling relation. We find there is a general agreement between the TM8 and TM9  $T$  measurements at a  $\lesssim 2.5\sigma$  level, with  $\xi = -0.05$ . Their scaling relation parameters for the full band fit are  $A = -0.020 \pm 0.015$ ,  $B = 0.921 \pm 0.038$ , and  $\sigma_{\text{tot}} = 0.193 \pm 0.010$ , while there is no intrinsic scatter. The agreement improves to  $\lesssim 2\sigma$  for the soft band, mostly due to the increase of measurement uncertainties.

Even though it is not statistically significant, TM9 measures slightly lower  $T$  than TM8 for  $T \gtrsim 3$  keV clusters (5% and 10% difference for  $T_{\text{TM8}} = 3$  keV and  $T_{\text{TM8}} = 6$  keV respectively). To ensure our findings are insensitive to this small TM9 effect, we refit the eROSITA-Chandra and eROSITA-XMM-Newton scaling relations excluding TM9 for the full and soft bands. We find very small differences with the default analysis. For the eROSITA-Chandra and eROSITA-XMM-Newton scaling relations both  $A$  and  $B$  change by  $\lesssim 2\%$  and  $\lesssim 2.5\%$  respectively. Consequently, TM9 does not introduce any bias to the  $T$  comparisons.

#### 8.4. Bias from non-Gaussian scatter and $T_{\text{eROSITA}}$ uncertainties

Due to the decrease of eROSITA's effective area at  $\gtrsim 2$  keV, clusters with higher  $T_{\text{eROSITA}}$  show larger uncertainties  $\sigma_{T_{\text{eROSITA}}}$ . For similar Chandra or XMM-Newton  $T$ , upscattered  $T_{\text{eROSITA}}$  show higher uncertainty on average than downscattered  $T$  values, making the total scatter slightly non-Gaussian. If clusters with truly high, upscattered  $T_{\text{eROSITA}}$  carry larger statistical uncertainties, the fit will give more weight to lower, downscattered  $T$  data points, shifting the best-fit relation away from the 1:1 relation. To test if this non-Gaussianity of  $\sigma_{T_{\text{eROSITA}}}$  has a significant effect on the scaling relation constraints, we refit the eROSITA-Chandra/XMM-Newton scaling relations for all bands, without taking into account  $\sigma_{T_{\text{eROSITA}}}$ , hence, we assign the same weight to all data points.

For the eROSITA-Chandra cross-calibration,  $A$  increases by  $\approx 0.007 - 0.013$  dex (1.5 – 3% in linear space) for all bands.  $B$  remains almost unchanged for the full and soft bands while it decreases by 3% for the hard band.

For the eROSITA-XMM-Newton cross-calibration the effect of non-Gaussianity is stronger.  $A$  increases by 0.044 dex (10%), 0.059 dex (13.5%), and 0.032 dex (7.6%) for the full, soft, and hard bands respectively.  $B$  increases by 1.4% and 0.3% for the full and soft bands and by 24% for the hard band. Non-Gaussianity has no significant effect on  $B$  for the full and soft bands. However, it causes an underestimation of  $A$ , resulting in an overestimation of the cross-calibration differences between eROSITA and XMM-Newton. Nevertheless, given the parameter uncertainties, this shift of  $A$  is within  $\lesssim 2\sigma$  from the default analysis. Of course the performed test here is quite conservative and demonstrates the maximum impact of non-Gaussianity possible.

To conclude, the non-Gaussianity of  $\sigma_{T_{\text{eROSITA}}}$  does not introduce any significant bias in the scaling relations between eROSITA and Chandra. On the other hand, it does partially overestimate the discrepancy between eROSITA and XMM-Newton, however, not at a statistically significant level. Moreover, this overestimation bias cannot fully alleviate the tension between  $T_{\text{eROSITA}}$  and  $T_{\text{XMM}}$  values. Non-Gaussianity effects become less relevant as more eROSITA counts are available for determining  $T_{\text{eROSITA}}$  and the  $T_{\text{eROSITA}}$  measurement uncertainties become smaller than the intrinsic scatter.

#### 8.5. Selection bias due to low $T/\sigma_T$

Due to its low sensitivity at  $\gtrsim 2.5$  keV, eROSITA returned a  $T/\sigma_T < 1$  measurement for 4% of the Chandra and 12% of the XMM-Newton cluster  $T$  for the full and soft bands. For the hard band, this fraction increased to 37% and 58% respectively. These clusters were excluded from the default analysis. With eROSITA, high  $T$  clusters are more likely to show lower  $T/\sigma_T$  on average than low  $T$  clusters for the same counts. Conse-

quently, excluding low  $T/\sigma_T$  measurements might lead to preferentially select clusters for which  $T_{\text{eROSITA}}$  was measured low. This selection effect could potentially shift the scaling relations further away from the equality line. To test this, we refit the scaling relations while considering all  $T$  measurements independently of their  $T/\sigma_T$  value.

The newly added data points have nearly no effect on the eROSITA-Chandra scaling relations for the full and soft bands. Both the new  $A$  and  $B$  best-fit values increase by  $< 1\%$  compared to the default best-fit values. This occurs since the added  $T/\sigma_T < 1$  measurements only marginally increase the sample size compared to the default case. Additionally, they carry very little statistical weight. For the hard band, the overall effect on  $A$  and  $B$  is similar, increasing only by 3% and 1% respectively. In all bands, the total scatter almost doubles when the low  $T/\sigma_T$  values are added to the sample.

For the eROSITA-XMM-Newton scaling relations in the full and soft bands, both  $A$  and  $B$  once again change by  $< 1\%$  compared to the default best-fit values. For the hard band, the sample size increases significantly. Nevertheless,  $A$  decreases by 4% while  $B$  increases by 9.5%. These changes are within  $0.5\sigma$  and do not practically improve the agreement between eROSITA and XMM-Newton.

It is evident that the data selection of  $T/\sigma_T > 1$  measurements introduces no significant bias to the final results, while it reduces the total scaling relation scatter. However, it is possible that when future eRASS data are used, more high- $T_{\text{eROSITA}}$  measurements will have higher  $T/\sigma_T$ , and hence, a larger effect on the best-fit scaling relations. This might cause the latter to shift somewhat closer to the equality line. Nonetheless, as shown in Sect. 8.4, this is unlikely to alleviate the cross-calibration differences between eROSITA and Chandra/XMM-Newton.

### 8.6. eROSITA's half-energy width and PSF effects

The on-axis half-energy width (HEW) of eROSITA is  $\approx 15.5 - 16.5''$  between 1.49 keV and 8.04 keV (Predehl et al. 2021). For the eROSITA survey data, such as eRASS1, the average HEW increases to  $\approx 26 - 29''$  (Brunner et al. 2022). This is only slightly larger than the XMM-Newton on-axis HEW ( $\approx 15 - 16''$ ), but significantly larger than the Chandra on-axis HEW ( $\approx 0.5 - 1''$ ). If the spectra extraction regions are not significantly larger than eROSITA's HEW then the emission from the cluster core might scatter to the core-excised annulus spectra. At the same time, Chandra would not suffer from this due to its much lower HEW. For cool core clusters, this would bias the core-excised  $T$  toward lower values. This is a potential problem for distant clusters with small apparent  $R_{500}$ . However, our sample consists of nearby clusters with large apparent  $R_{500}$ . Characteristically, the median apparent radius of the cluster cores ( $< 0.2R_{500}$ ) is  $2.3'$ , which is  $5\times$  the eROSITA survey HEW. At the same time, only four clusters of the eROSITA-Chandra comparison subsample (3.6% of the subsample) have a cluster core of  $< 65''$ , that is,  $\lesssim 2.5\times$  the eROSITA survey HEW. These clusters do not show any special behavior compared to the rest of the sample. In conclusion, it is clear that the eROSITA HEW has nearly no effect on the eROSITA-Chandra  $T$  comparison. The same conclusion was reached by S15 for the XMM-Newton-Chandra  $T$  comparison and a similar cluster population.

### 8.7. Consistency with past studies and indirect eROSITA comparison with other X-ray telescopes

The only previous eROSITA cross-calibration test using a cluster sample was performed against XMM-Newton by Turner et al. (2022), who used  $T$  measurements from eight common eFEDS and XCS clusters. Despite the very small number of available data points and the different energy ranges used for eROSITA and XMM-Newton spectral analysis, they found  $T_{\text{eROSITA}} = 0.75^{+0.10}_{-0.08} \times T_{\text{XMM}}$ , for a fixed slope of unity. This is completely consistent with our result. As discussed in Sect. 1, there are also a few studies that used individual cluster  $T$  measurements to compare eROSITA with other instruments (e.g., Liu et al. 2023). However, a direct comparison of our results with these studies is not helpful, since single  $T$  comparisons can scatter significantly around the average behavior we present in this work.

Furthermore, based on our findings, we can 1) perform an indirect consistency test with past Chandra-XMM-Newton cross-calibration studies and 2) evaluate the eROSITA cross-calibration with other X-ray telescopes such as Suzaku and NuSTAR.

Using the full band eROSITA-Chandra and eROSITA-XMM-Newton scaling relations, we can indirectly constrain the Chandra-XMM-Newton  $T$  scaling relation and compare it with the findings of S15 (after adjusting for the pivot points S15 used). We find

$$\log_{10} T_{\text{XMM}} \approx 0.010 + 0.946 \times \log_{10} T_{\text{Chandra}}, \quad (9)$$

entirely consistent with S15 within the  $1\sigma$  uncertainties.

Kettula et al. (2013) found that Suzaku returned  $\sim 12\%$  lower  $T$  than the PN detector onboard XMM-Newton. Based on that, one can predict that eROSITA and Suzaku  $T$  should be closer compared to the other instruments, especially at lower  $T$  where they should be comparable. However, eROSITA is still expected to return lower  $T$  than Suzaku by  $\sim 10 - 15\%$  for  $T = 7$  keV clusters. Nevertheless, it is not trivial to draw robust conclusions due to the very limited sample of Kettula et al. (2013), their use of PN-only data, and the different energy bands in which they performed the Suzaku-XMM-Newton cross-calibration. It is interesting to note here that, if multitemperature structure was the main cause of the observed  $T$  discrepancies across different instruments, Suzaku would be expected to return higher  $T$  than XMM-Newton (and comparable to Chandra), which is not the case.

Finally, Wallbank et al. (2022) reported  $\approx 10\%$  lower  $T$  from NuSTAR compared to Chandra for the 0.6-9.0 keV band and  $T \approx 10$  keV clusters. As a result, one would expect eROSITA to measure much lower  $T$  than NuSTAR for massive clusters. On the  $T \lesssim 2$  keV end, eROSITA is expected to return rather consistent  $T$  values with NuSTAR within  $\approx 3 - 5\%$ . As we stressed already, these predictions simply help us understand better what to expect from future studies, rather than providing a comparison between eROSITA, NuSTAR, and Suzaku.

### 8.8. Future improvements

The current analysis already put tight constraints in the eROSITA cross-calibration with Chandra and XMM-Newton and provides a good understanding of the photon energy and cluster mass dependence of the  $T$  discrepancy. These results will be highly valuable for future studies that wish to use eROSITA  $T$  combined with  $T$  values from other telescopes. Nonetheless, there is still room for several improvements to be made in the future.



First and foremost, the  $T_{\text{eROSITA}}$  measurement uncertainties are still large. Their decrease would result in a lower total scatter, improving the precision of the constraints. This will be achieved with the eRASS:4 data, where  $\sigma_{T_{\text{eROSITA}}}$  will be reduced by a factor of  $\sim 2$ . Additionally, the effects of the non-Gaussian scatter will also be better studied and accounted for, since higher  $T_{\text{eROSITA}}$  will carry lower uncertainties and higher statistical weight compared to the present work.  $T_{\text{break}}$  will also be better constrained when using a broken power law to fit the scaling relations.

The  $4\times$  more counts in the eRASS:4 data will also allow us to use narrower energy bands for the spectral analysis, for instance, 0.5–2 keV and 2–8 keV. Consequently, a better characterization of the effective area cross-calibration as a function of energy will be achieved, for example, by utilizing the stacked residual ratios methodology (Kettula et al. 2013). In this work, it was not possible to robustly constrain  $T_{\text{eROSITA}}$  using narrower energy bands due to the limited available counts. As a result, the soft and hard bands inevitably overlapped.

Given the higher number of counts in eRASS:4, a better characterization of the multiphase gas bias will also be achieved. Multitemperature emission models will be fit to the spectra, which will reduce any dependence of the observed  $T$  discrepancy on the different effective areas of the compared telescopes. Such fits were not possible in this study due to the limited number of counts in eRASS1. Moreover, eROSITA and XMM-Newton have similar effective area shapes in the 0.5 – 2 keV band. Therefore, when more available counts allow us to constrain  $T$  in this band, eROSITA and XMM-Newton should not show any systematic discrepancies due to the presence of multiphase gas and any discrepancies would be attributed to systematic calibration uncertainties.

Another interesting future test is the dependence of the comparison to the cluster redshift. The M20 sample used in this work is a low- $z$  sample with most clusters lying at  $z < 0.2$ . As the  $T$  comparison between eROSITA and Chandra/XMM-Newton depends on both the energy band and  $T$  (i.e., spectral shape), the  $T$  comparison might slightly change for different redshift ranges. In this work, it was not possible to perform such a test, since the redshift range is small and clusters with higher  $T$  are found at larger  $z$ . As a result, larger  $z$  would deviate more than low  $z$  due to the different cluster populations. The upcoming eRASS:4 data will allow for using similar cluster samples at different  $z$  to detect any possible redshift dependency of the eROSITA-Chandra/XMM-Newton cluster  $T$  comparison.

Finally, the eROSITA-XMM-Newton sample size will be increased. Due to the nature of the M20 sample, XMM-Newton data were available mostly for low flux (i.e., low eROSITA counts on average) clusters, and only for 51 of them. This resulted in 71 independent  $T_{\text{eROSITA}}$  and  $T_{\text{XMM}}$  (core and core-excised annulus). Given the vast availability of XMM-Newton cluster data and the deeper eRASS:4 data, we expect the eROSITA-XMM-Newton  $T$  scaling relations to significantly improve within the next years. A broken power law analysis will then become feasible for these scaling relations as well.

## 9. Summary and conclusions

In this work we provided the first-ever eROSITA-Chandra cross-calibration in the broad, soft, and hard X-ray energy bands, using the same spectral energy ranges and 186 independent galaxy cluster  $T$ , the largest sample used in such studies to date. In the same manner, we also provided the first eROSITA-XMM-Newton calibration in the soft and hard bands, and the first in

the broad band using the same spectral energy for both instruments and a much larger  $T$  sample than previously used. Our work offers robust conversion factors for the measured  $T$  between eROSITA, Chandra, and XMM-Newton.

Using a single power law fit, we found that eROSITA shows a strong discrepancy with Chandra, measuring 25% and 38% lower  $T_{\text{eROSITA}}$  for  $T_{\text{Chandra}} = 4.5$  keV and  $T_{\text{Chandra}} = 10$  keV respectively. Furthermore, we performed the first-ever (to our knowledge) broken power law fit in such a  $T$  cross-calibration scaling relation. We found the  $T$  where the power law breaks to be 2.7 keV and 1.7 keV for the full and soft band respectively. At lower  $T$ , the values of the two telescopes were consistent within  $\lesssim 5\%$ , with a slope close to unity. For  $T \gtrsim 6$  keV clusters, the broken power law further increased the tension between eROSITA and Chandra by a few percent. The hard band was the one that showed the largest discrepancy between the two instruments, with eROSITA returning  $\approx 25\text{--}60\%$  lower  $T_{\text{eROSITA}}$  for  $T_{\text{Chandra}} \approx 2 - 10$  keV.

eROSITA shows lower  $T$  than XMM-Newton as well, with the discrepancy being milder than the one with Chandra. For the full band, eROSITA measures 10 – 28% lower  $T_{\text{eROSITA}}$  for  $T_{\text{XMM}} \approx 2 - 7$  keV clusters, while there is a slightly better agreement for cooler systems. The (dis)agreement between the two instruments improves by a few percent for the soft band. The hard band was only loosely constrained due to the large measurement uncertainties, although it is obvious that eROSITA largely underestimates  $T$  compared to XMM-Newton in the hard band.

A wide range of possible systematics was explored. Namely, we looked for possible biases introduced by multitemperature gas structure, the degeneracy between the temperature and the metallicity parameters, the effect different levels of Galactic absorption have on the  $T$  constraints of different telescopes, the non-Gaussianity of the scatter and the correlation between  $T_{\text{eROSITA}}$  and its uncertainty, sample selection effects, and the use of eROSITA TM8 and TM9 data. We could not identify a specific systematic that had a strong effect on the eROSITA cross-calibration with Chandra and XMM-Newton, although more future work is needed to obtain conclusive results about some potential biases.

Overall, the soft band demonstrated a marginally improved agreement between instruments than the full band, whereas the hard band cross-calibration revealed significant discrepancies. Similarly, clusters with softer spectra and lower  $T$  showed much better agreement than clusters with harder spectra and high  $T$ . Subsequently, we conclude that eROSITA's effective area calibration is more comparable to Chandra and XMM-Newton for soft X-ray energies, though there is still systematic bias present. Our findings further point to a larger systematic bias in the eROSITA's cross-calibration with Chandra and XMM-Newton at harder energies. It is possible that this bias is overestimated due to the lower statistical weight that high  $T_{\text{eROSITA}}$  carry given the shallow eRASS1 data. For now, in line with earlier studies, we conclude that these discrepancies are attributed to systematic effective area calibration uncertainties.

Finally, our work offers the first robust conversion factors of spectroscopic eROSITA  $T$  to XMM-Newton and Chandra  $T$ . Additionally, we offer conversion factors between the official eRASS1 cluster catalog  $T$  and core/core-excised Chandra and XMM-Newton  $T$ . All these will enable the simultaneous use of eROSITA cluster  $T$  with values coming from the other two telescopes. Given the unprecedented volume of cluster data eRASS1 (and eventually eRASS:4 and eRASS:8) will provide, these conversion factors are expected to be of utter importance for future cluster studies.



## Acknowledgements

We thank the anonymous referee for their constructive and insightful comments. This work is based on data from eROSITA, the soft X-ray instrument aboard SRG, a joint Russian-German science mission supported by the Russian Space Agency (Roskosmos), in the interests of the Russian Academy of Sciences represented by its Space Research Institute (IKI), and the Deutsches Zentrum für Luft- und Raumfahrt (DLR). The SRG spacecraft was built by Lavochkin Association (NPOL) and its subcontractors, and is operated by NPOL with support from the Max Planck Institute for Extraterrestrial Physics (MPE). The development and construction of the eROSITA X-ray instrument was led by MPE, with contributions from the Dr. Karl Remeis Observatory Bamberg & ECAP (FAU Erlangen-Nuernberg), the University of Hamburg Observatory, the Leibniz Institute for Astrophysics Potsdam (AIP), and the Institute for Astronomy and Astrophysics of the University of Tübingen, with the support of DLR and the Max Planck Society. The Argelander Institute for Astronomy of the University of Bonn and the Ludwig Maximilians Universität Munich also participated in the science preparation for eROSITA. The eROSITA data shown here were processed using the eSASS software system developed by the German eROSITA consortium. K.M. acknowledges support in the form of the X-ray Oort Fellowship at Leiden Observatory. G.S. acknowledges support through the Chandra grant GO5-16126X. A.V. acknowledges funding by the Deutsche Forschungsgemeinschaft (DFG, German Research Foundation) – 450861021.

## References

- Akritas, M. G. & Bershad, M. A. 1996, *ApJ*, 470, 706  
Arnaud, K. A. 1996, in *Astronomical Society of the Pacific Conference Series*, Vol. 101, *Astronomical Data Analysis Software and Systems V*, ed. G. H. Jacoby & J. Barnes, 17  
Arnaud, M., Pratt, G. W., Piffaretti, R., et al. 2010, *A&A*, 517, A92  
Asplund, M., Grevesse, N., Sauval, A. J., & Scott, P. 2009, *ARA&A*, 47, 481  
Borm, K., Reiprich, T. H., Mohammed, I., & Lovisari, L. 2014, *A&A*, 567, A65  
Brunner, H., Liu, T., Lamer, G., et al. 2022, *A&A*, 661, A1  
Bulbul, E., Chiu, I. N., Mohr, J. J., et al. 2019, *ApJ*, 871, 50  
Bulbul, E., Liu, A., Kluge, M., et al. 2024, Accepted in *A&A*  
Buote, D. A. 2002, *ApJ*, 574, L135  
Cash, W. 1979, *ApJ*, 228, 939  
Eckert, D., Jauzac, M., Shan, H., et al. 2015, *Nature*, 528, 105  
Humphrey, P. J., Liu, W., & Buote, D. A. 2009, *ApJ*, 693, 822  
Kettula, K., Nevalainen, J., & Miller, E. D. 2013, *A&A*, 552, A47  
Kuntz, K. D. & Snowden, S. L. 2008, *A&A*, 478, 575  
Liu, A., Bulbul, E., Ghirardini, V., et al. 2022, *A&A*, 661, A2  
Liu, A., Bulbul, E., Ramos-Ceja, M. E., et al. 2023, *A&A*, 670, A96  
Lovisari, L., Reiprich, T. H., & Schellenberger, G. 2015, *A&A*, 573, A118  
Lovisari, L., Schellenberger, G., Sereno, M., et al. 2020, *ApJ*, 892, 102  
Luo, B., Brandt, W. N., Xue, Y. Q., et al. 2017, *ApJS*, 228, 2  
McCammon, D., Almy, R., Apodaca, E., et al. 2002, *The Astrophysical Journal*, 576, 188  
Merloni, A., Lamer, G., Liu, T., et al. 2024, 682, A34  
Merloni, A., Predehl, P., Becker, W., et al. 2012, *ArXiv e-prints* [arXiv:1209.3114]  
Mernier, F., de Plaa, J., Werner, N., et al. 2018, *MNRAS*, 478, L116  
Migkas, K., Pacaud, F., Schellenberger, G., et al. 2021, *A&A*, 649, A151  
Migkas, K., Schellenberger, G., Reiprich, T. H., et al. 2020, *A&A*, 636, A15  
Mittal, R., Hicks, A., Reiprich, T. H., & Jaritz, V. 2011, *A&A*, 532, A133  
Nevalainen, J., David, L., & Guainazzi, M. 2010, *A&A*, 523, A22  
Piffaretti, R., Arnaud, M., Pratt, G. W., Pointecouteau, E., & Melin, J.-B. 2011, *A&A*, 534, A109  
Pillepich, A., Porciani, C., & Reiprich, T. H. 2012, *MNRAS*, 422, 44  
Pratt, G. W., Croston, J. H., Arnaud, M., & Böhringer, H. 2009, *A&A*, 498, 361  
Predehl, P., Andritschke, R., Arefiev, V., et al. 2021, *A&A*, 647, A1  
Ramos-Ceja, M. E., Pacaud, F., Reiprich, T. H., et al. 2019, *A&A*, 626, A48  
Reiprich, T. H., Basu, K., Ettori, S., et al. 2013, *Space Sci. Rev.*, 177, 195  
Riva, G., Ghizzardi, S., Molendi, S., et al. 2022, *A&A*, 665, A81  
Sanders, J. S., Biffi, V., Brüggemann, M., et al. 2022, *A&A*, 661, A36  
Sanders, J. S., Fabian, A. C., Russell, H. R., & Walker, S. A. 2018, *MNRAS*, 474, 1065

- Schellenberger, G. & Reiprich, T. H. 2017a, *MNRAS*, 469, 3738  
Schellenberger, G. & Reiprich, T. H. 2017b, *MNRAS*, 471, 1370  
Schellenberger, G., Reiprich, T. H., Lovisari, L., Nevalainen, J., & David, L. 2015, *A&A*, 575, A30  
Snowden, S. L., Egger, R., Freyberg, M. J., et al. 1997, *ApJ*, 485, 125  
Sunyaev, R., Arefiev, V., Babyshkin, V., et al. 2021, *A&A*, 656, A132  
Turner, D. J., Giles, P. A., Romer, A. K., et al. 2022, *MNRAS*, 517, 657  
Veronica, A., Reiprich, T. H., Pacaud, F., et al. 2024, *A&A*, 681, A108  
Veronica, A., Su, Y., Biffi, V., et al. 2022, *A&A*, 661, A46  
Wallbank, A. N., Maughan, B. J., Gastaldello, F., Potter, C., & Wik, D. R. 2022, *Monthly Notices of the Royal Astronomical Society*, 517, 5594  
Werner, N., Finoguenov, A., Kaastra, J. S., et al. 2008, *A&A*, 482, L29  
Whelan, B., Veronica, A., Pacaud, F., et al. 2022, *A&A*, 663, A171  
Willingale, R., Starling, R. L. C., Beardmore, A. P., Tanvir, N. R., & O'Brien, P. T. 2013, *MNRAS*, 431, 394  
ZuHone, J., Bahar, Y. E., Biffi, V., et al. 2023, *A&A*, 675, A150

## Appendix A: Additional material and tests

### Appendix A.1: Free-to-vary metal abundance and temperature distributions

In Table A.1 we present the best-fit scaling relation parameters when  $Z$  is left free to vary, as explained in Sect. 8.1. As discussed earlier, the general behavior of the scaling relations remains unaffected, with only a slight increase in the scatter being observed. Thus, the metallicity value treatment is not important for the temperature comparison between different instruments.

In Fig. A.2 we show the Chandra and XMM-Newton  $T$  distributions of cluster core and core-excised regions, as discussed in Sect. 8.2.1. The  $T$  distributions are very similar. Hence, the core and core-excised cross-calibration results of these two subsamples are directly comparable and any observed differences should not be attributed to a different  $T$  range.

### Appendix A.2: $\chi^2$ -statistic bias compared to C-statistic

The  $\chi^2$ -statistic assumed Gaussian distribution of spectral counts and can return biased  $T$  values during spectral fitting, while the C-statistic is based on Poissonian count distributions and it is known to return nearly unbiased  $T$  results. However, the  $\chi^2$  bias reduces in amplitudes as the number of available counts increases per bin and in total since the counts distribution can be well approximated by a Gaussian distribution. Due to that, using the  $\chi^2$ -statistic for fitting X-ray spectra is considered standard practice in X-ray astronomy. In this work, the XMM-Newton and Chandra spectra we use typically contain  $\geq 10,000$ ,  $\geq 8,000$ , and  $\geq 5,000$  counts for the full, soft, and hard bands respectively. As a result, adopting the  $\chi^2$ -statistic (to be consistent with the full band results from M20) should not introduce strong biases in the best-fit  $T$  compared to the C-statistic. We confirm this by fitting 10 randomly selected full band XMM-Newton spectra by using the `cstat` option in XSPEC. The average shift in the best-fit  $T$  is  $\approx 0.6\sigma$ , or  $\approx 2.5\%$ . This is consistent with what was shown in Veronica et al. (2022), where they observed similar  $T$  shifts by changing between the above-mentioned statistics.

Humphrey et al. (2009) explored this issue in detail. They used simulated thermal plasma emission spectra and fitted them with Chandra to determine the bias of the  $\chi^2$ - and C-statistics as a function of the available counts and thermal plasma properties. They found that, while the amplitude of the bias decreases with increasing counts, the *significance* of the  $T$  shift increases until  $\sim 10^5$  counts (Fig. 2 in that paper). This occurs because, as counts increase,  $\sigma_T$  drops faster than the absolute  $T$  bias. For our number of counts in the XMM-Newton and Chandra spectra, Humphrey et al. (2009) predicts a  $T$  bias of  $\sim 0.5-1\sigma$ . To test the effect such a bias would have in the constrained scaling relations, we refit the latter in all bands for both the eROSITA-Chandra and eROSITA-XMM-Newton comparisons, but we increase  $T_{\text{Chandra}}$  and  $T_{\text{XMM}}$  by  $\sim 0.5 - 1\sigma$ <sup>16</sup>. The shift in the  $1\sigma$  contours of all scaling relations is displayed in Fig. A.1. The best-fit parameters change by  $\leq 1.1\sigma$  for all scaling relations. The largest change is found for both the soft band comparisons, where  $A$  changes by 0.01 dex (2.3%) and 0.013 dex (3%) for the eROSITA-Chandra and eROSITA-XMM-Newton scaling relations respectively. The slope  $B$  changes by 1.7% for both relations.

The minimal effect of this temperature shift, since small changes in  $T_{\text{XMM}}$  and  $T_{\text{Chandra}}$  are negligible compared to the uncertainties of  $T_{\text{eROSITA}}$  for most clusters. Additionally, the slope

of the relations ( $B$   $0.65 - 0.85 < 1$ ) further minimizes the effect that small  $T_{\text{XMM}}$  and  $T_{\text{Chandra}}$  changes have on the results. Consequently, the exact statistic used to fit the XMM-Newton and Chandra spectra does not affect the conclusions of this work.

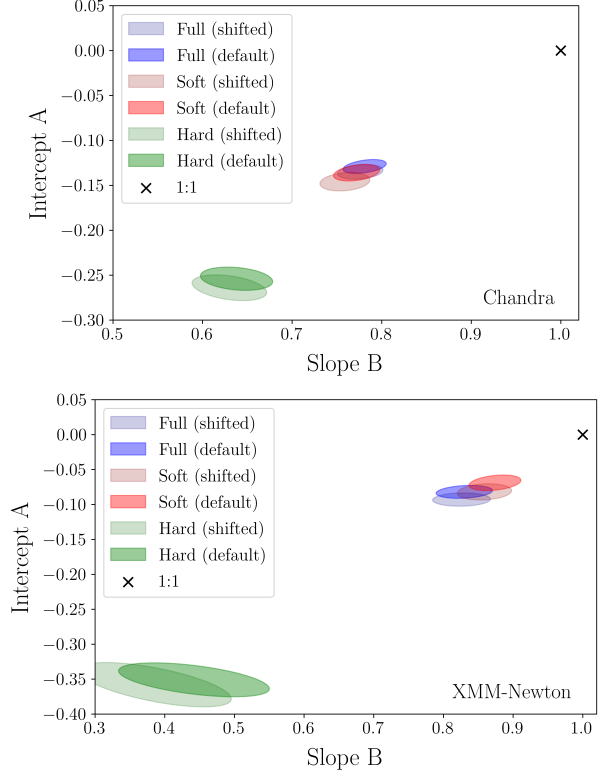


Fig. A.1:  $1\sigma$  confidence levels for the eROSITA-Chandra (top) and eROSITA-XMM-Newton (bottom) scaling relations, for the full (blue), soft (red), and hard (green) bands. The more opaque ellipses correspond to the default results while the more transparent ellipses correspond to the best-fit results when  $T_{\text{Chandra}}$  and  $T_{\text{XMM-Newton}}$  are increased by  $\sim 0.5 - 1\sigma$ , as described in Sect. A.2.

### Appendix A.3: Outliers in the eROSITA-XMM-Newton hard band comparison

There are two strong outliers in the eROSITA-XMM-Newton hard band comparison; the core of A0602 ( $T_{\text{XMM}} = 2.850^{+0.158}_{-0.122}$ ) and the annulus of A2721 ( $T_{\text{XMM}} = 6.781^{+0.703}_{-0.553}$ ). Both of these regions return  $T_{\text{eROSITA}} < 0.3$  keV with  $T/\sigma_T > 2$ . Both hard band spectra have very low eROSITA counts and higher  $T$  models return rather consistent fits as well; thus, their obtained  $T_{\text{eROSITA}}$  uncertainties seem to be underestimated. Including these two data points, the LMM slope decreases to  $B = 0.324^{+0.361}_{-0.314}$  while the intrinsic scatter increases by a factor of five. Thus, these outliers have a strong effect on the best-fit results. The core  $T$  of A0602 is  $\approx 1.9$  keV in the full and soft bands while the annulus  $T$  of A2721 could not be constrained with eROSITA in these bands. Consequently, based on all the above, their hard band  $T$  seem to be problematic and they were excluded.

<sup>16</sup> The exact factor depends on the average number of counts in that band per instrument, and it is based on Fig. 2 of Humphrey et al. (2009).

Table A.1: Same as in Table 1, but leaving  $Z$  free to vary during the eROSITA spectral fits.

Comparison	Band	$A$	$B$	$\sigma_{\text{intr}}$	$\sigma_{\text{tot}}$	$\xi$
eROSITA-Chandra	Full	$-0.162^{+0.009}_{-0.008}$	$0.758^{+0.019}_{-0.016}$	$0.041 \pm 0.015$	$0.147 \pm 0.007$	-1.50
	Soft	$-0.170 \pm 0.010$	$0.734 \pm 0.018$	$0.034 \pm 0.017$	$0.143 \pm 0.009$	-1.67
	Hard	$-0.252 \pm 0.022$	$0.676 \pm 0.079$	$0.132 \pm 0.022$	$0.273 \pm 0.016$	-1.51
eROSITA-XMM-Newton	Full	$-0.113^{+0.023}_{-0.020}$	$0.734^{+0.110}_{-0.096}$	$0.105 \pm 0.024$	$0.227 \pm 0.015$	-0.74
	Soft	$-0.077^{+0.029}_{-0.026}$	$0.772^{+0.108}_{-0.092}$	$0.075 \pm 0.025$	$0.193 \pm 0.016$	-0.53
	Hard	$-0.339^{+0.044}_{-0.041}$	$0.458^{+0.261}_{-0.194}$	$0.160 \pm 0.059$	$0.334 \pm 0.035$	-1.80

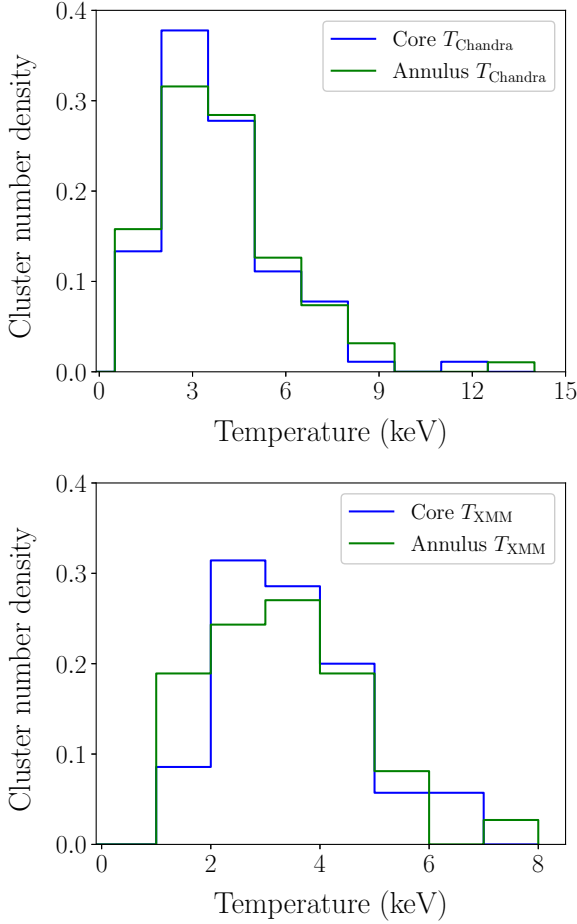


Fig. A.2: Histogram of core (blue) and core-excise (green) temperature values for Chandra (left) and XMM-Newton (right). The two distributions are very similar for both instruments.

#### Appendix A.4: Multitemperature fits with single $T$ models for the hard band

We repeat the analysis of Sect. 8.2.1, focusing on the hard band this time. As shown in Fig. A.3, the three instruments return very similar single  $T$  constraints for all  $2T$  combinations. Although the  $T_{\text{eROSITA}}$  uncertainties are very large and only  $< 2\sigma$  away from the observed cross-calibration differences, the general trend

does not seem to explain the observed  $T$  tension, especially between eROSITA and Chandra.

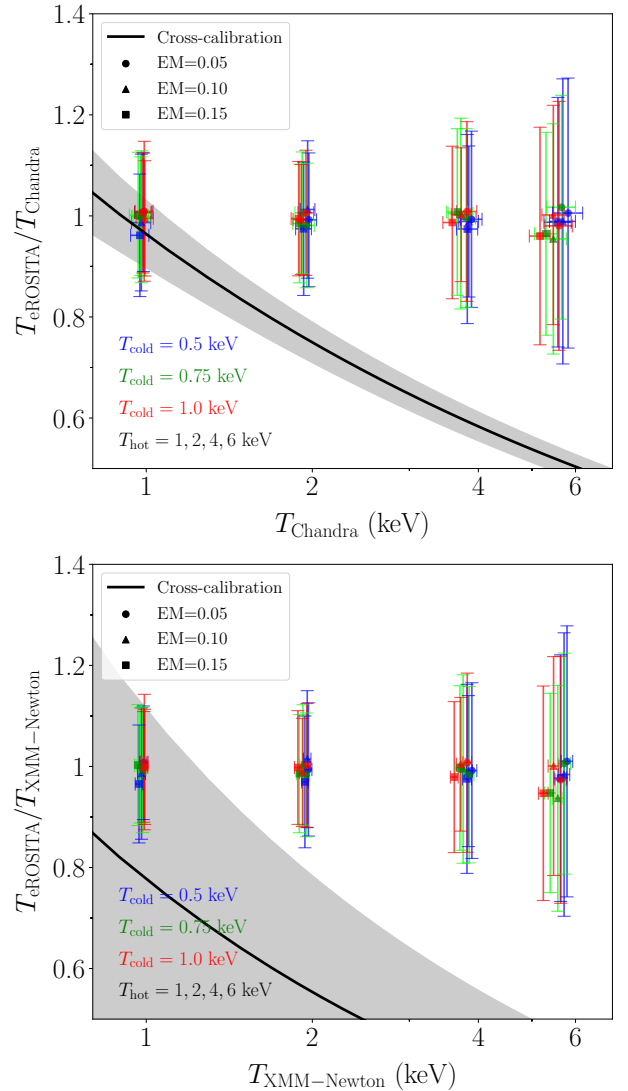


Fig. A.3: Same as in Fig. 9, but for the hard band fits.